https://doi.org/10.5194/egusphere-2026-3588
Preprint. Discussion started: 4 August 2026

Physical-Statistical Retrieval of SWE and Snow Depth in Forested Areas from Airborne X And Ku-Band SAR Measurements

Siddharth Singh[1], Carrie Vuyovich[2] Ana P. Barros[1]

[1]Department of Civil and Environmental Engineering, University of Illinois at Urbana- Champaign, Urbana, Illinois, USA
[2]NASA Goddard Space Flight Center - Greenbelt, MD

Correspondence to: Ana P. Barros (barros@illinois.edu)

Abstract

This study presents a physical-statistical Snow Water Equivalent (SWE) retrieval framework in forested areas using dual-frequency X- and Ku-band SAR airborne measurements. The methodology builds on previous work coupling snow hydrology and microwave propagation and backscatter models and introduces a parameterization of microwave propagation and scattering within the forest canopy based on the Water Cloud Model (WCM) modified to account for canopy closure effects. The retrieval framework was applied to SnowSAR measurements from four flights over Grand Mesa, Colorado and its performance was evaluated against snow pit observations and LiDAR snow depth measurements. Prior distributions of snowpack properties were generated using a multilayer snow hydrology model (MSHM) forced with Numerical Weather Prediction (NWP) analysis data. SAR measurements were spatially averaged to 90m and 30m resolution for retrieval. Prior distributions of vegetation and ground parameters were initialized using Ku-HH measurements, with effective soil and vegetation parameters estimated for frozen conditions. Soil parameters were estimated in open areas and spatially interpolated to nearby forested areas using ordinary kriging. SWE and snow depth retrievals for forested pixels at 90 m resolution were considered successful by accepting a relative residual backscatter (RRB) tolerance in the Bayesian optimization up to 30% for individual pixels with incidence angles between 30°–50° along SnowSAR flight paths. Successful retrievals capture both the mean and spatial variance of snowpack properties across the Grand Mesa plateau consistent with the LiDAR survey with RRB generally below 5%. Validation against collocated LiDAR snow depth and snow pit SWE measurements from the SnowEx'17 campaign show a root mean square error (RMSE) of 0.033 m (< 8% of maximum SWE for pits) and improved spatial patterns compared to snow hydrology predictions driven by NWP alone. The errors are larger in pixels with mixed land-cover (e.g., forest-grassland boundaries, land-margins of frozen ponds and lakes, and mixed forest) due to increased uncertainty in the estimation of vegetation parameters. Absolute relative differences (ARD) between LiDAR snow depth and SAR snow depth retrievals are below 10% for 62% of the forested pixels at 90 m resolution, and the fraction of successful retrievals increases to 82% for ARD < 20%. Retrievals at 30 m resolution achieve dramatic improvement with 78% of the retrievals for ARD < 10% due to reduced mixed land-cover uncertainty. These results demonstrate the feasibility of dual-frequency Bayesian SWE retrieval in forested landscapes by combining physical modeling with remote sensing at high spatial resolution enabled by SAR.

Keywords: Snow Water Equivalent; Bayesian retrieval; X- and Ku-band SAR; Water Cloud Model; Canopy closure; Snow hydrology modeling; SnowEx Grand Mesa

1. Introduction

Snow accumulation changes in cold regions such as the Arctic are monitored with great interest as they reflect concerted changes in precipitation patterns as well as regional weather (Lee et al., 2021; Shi and Liu 2021; Swiatnek et al., 2024; Kacimi and Kwok 2022; Pongcraz et al., 2024; Gottlieb and Mankin 2024). Snow cover and snowpack microphysical properties govern terrestrial albedo over large regions of the world and thus play a key role in regulating the planet's energy budget (Fassnacht et al., 2016; Xu and Dirmeyer 2013; Jennings and Molotch 2020). Snowpacks represent an important form of transient water storage in the cold season followed by melt and runoff in the warm season (Rodell et al., 2004; Lim et al., 2022; Mazzoti et al., 2024). Monitoring and predicting snowpack properties is essential for a myriad of applications from water resources management to agriculture production to flood response and mitigation (Gardener et al. 2013; Semdeni Davies 2004; Falk and Lin 2021).

https://doi.org/10.5194/egusphere-2026-3588
Preprint. Discussion started: 4 August 2026

Remote sensing of snowpack properties relies on Mie scattering theory, which describes the interaction between electromagnetic waves (EMW) and particles based on their relative sizes (Aoki et al., 2000; Hall et al., 2004; Tsang et al., 2007). Thus, the EM wavelength and the diameter of the particle (D) determine the type of information gathered. When the EM wavelength (λ) is much smaller than the particle diameter D ($\lambda \ll D$), surface reflectance is the dominant scattering process. Conversely, when the wavelength is equal to or larger than the particle diameter ($\lambda \geq D$), volumetric scattering is dominant, revealing information about the internal structure of the snowpack. The trade-off between surface and volume scattering is crucial in selecting and combining appropriate wavelengths for remote sensing applications. Previous research has demonstrated value in the combination of X and Ku-band backscatter measurements to quantify snow mass properties from volume backscatter (Singh et al., 2024; Boyd et al., 2022; Tsang et al., 2022).

Snow water equivalent (SWE), obtained as the product of snow depth and snow density, represents the amount of water stored in a snowpack if melted completely. Thus, to estimate SWE is to estimate snow water resources. Statistical models that integrate SWE estimates from microwave backscatter observations with ground-based measurements, often through cost minimization or data assimilation approaches, have been widely employed to estimate SWE at high spatial resolution (Mote et al., 2005; Li et al., 2017; Zhu et al., 2021)). However, purely statistical, or machine-learning approaches frequently show reduced accuracy when extrapolated to higher-resolution or more heterogeneous landscapes, where scale and physical complexity differ from the training domain (Hernanz 2024; Slater et al., 2025). This issue will become more important with the increasing availability of high-resolution remote sensing data (Wrzesien et al., 2017; Sabetghadam et al., 2025; Boueshagh et al., 2025). Data assimilation into snow hydrology models provides a general path for SWE estimation constrained by physical principles (Stur, et al., 2010; Cao and Barros 2020).

Cao and Barros (2020) integrated the Multilayered Snow Hydrology Model (MSHM) earlier developed by Kang and Barros (2011 a and b) and simulates the temporal evolution of snowpacks and captures detailed changes in snow stratigraphy and internal structure with the Microwave Emission Model of Multilayered Snowpacks (MEMLS, Proksch et al., 2015) for forward simulations of snowpack microstructure. Pan et al. (2023) implemented MEMLS in a Bayesian framework, referred to as BASE-AM, to estimate SWE from active microwave backscatter measurements. Building on these, Singh et al. (2024) modified the BASE-AM algorithm to derive snowpack priors from MSHM simulations driven by weather forecasts and to improve ground backscatter estimates for frozen soils. They applied the modified algorithm to retrieve SWE from Ku- and X-band SnowSAR observations from the NASA SnowEx'17 campaign in Grand Mesa, Colorado achieving an RMSE of less than 7% when compared with snow pit observations in open snow-covered grasslands.

https://doi.org/10.5194/egusphere-2026-3588
Preprint. Discussion started: 4 August 2026

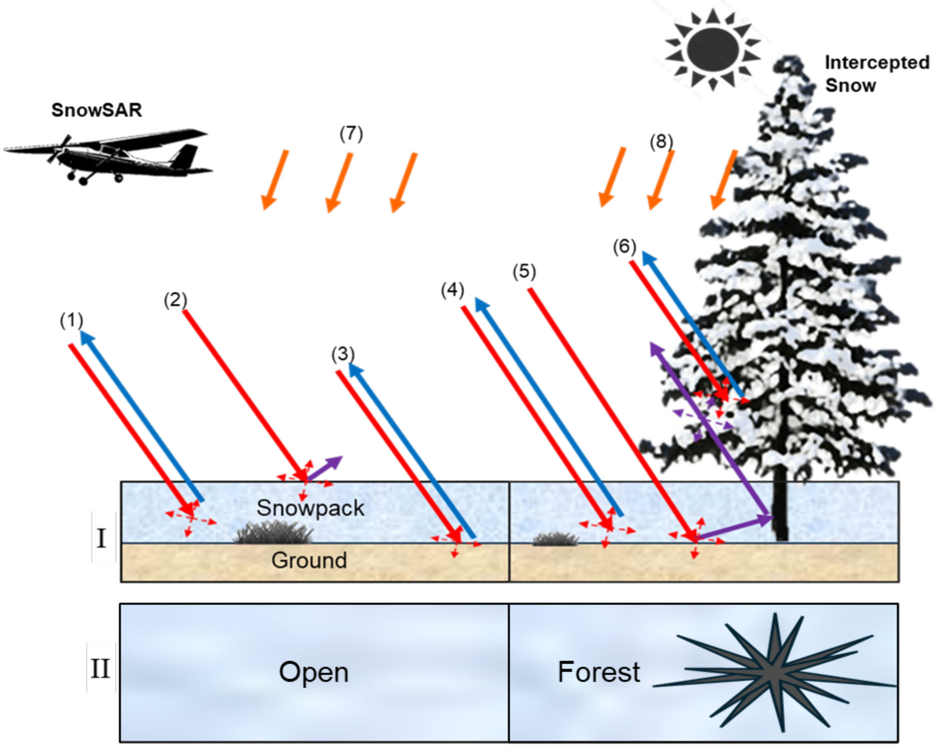

Figure 1 - I) Side view of scattering mechanisms for neighboring grassland and forest pixels submerged by snow and snowpack over bare soil or rock: (1) Volume Backscatter σ_{vol}; (2) surface backscatter σ_{surf}; (3) background backscatter at the snow-ground interface σ_{bkg}; (4) Volume Backscatter σ_{vol} not affected by vegetation in a forest designated pixel (5) snowpack-ground-canopy-tree interaction with one way vegetation backscatter (6) Two way vegetation backscatter σ_{veg} at high frequency (7) Incoming solar radiation in open area (8) Solar radiation in forest pixel requiring correction. II) Top view of pixels with illustrating canopy closure.

The scattering behavior of active microwaves in forested snowpacks is very complex including interactions among vegetation, snowpack, submerged vegetation, and ground (Figure 1; Mahat et al., 2012; Essery et al., 2024) resulting in strong attenuation of backscatter and challenging separation of scattering and attenuation sources (Cho et al., 2023; Lemmetyinen et al., 2022). The goal of this study is to extend the physical-statistical retrieval framework from Singh and Barros 2024 to forested environments and assess its utility to support SAR remote-sensing of snow. Retrieving SWE in forested landscapes remains a major challenge for snow remote sensing, yet it is essential because forests account for one-third of Earth's seasonal snow-covered area (Bonnell et al., 2024). For this purpose, in this work we modify the algorithm presented by Singh et al. (2023) to include canopy processes and apply the modified physical-statistical retrieval framework for forested pixels only.

2. Study Area and Datasets

The study is conducted over Grand Mesa, Colorado, a high-elevation plateau situated approximately 2,000 m above surrounding lowlands and bordered by ridges rising to 500 m. Grand Mesa experiences an alpine climate with persistent snowfall outside of July and August. The region exhibits heterogeneous land cover, with grasslands in the west and a mix of evergreen and deciduous forests toward the east, interspersed with wetlands, especially across ecotonal zones. Land cover classification is based on the National Land Cover Dataset (NLCD) and resampled to 90 m using nearest neighbor interpolation to support retrievals at that scale, consistent with the methodology described

https://doi.org/10.5194/egusphere-2026-3588
Preprint. Discussion started: 4 August 2026

in Singh et al. (2024). Hourly albedo is derived from 12.5 km National Land Data Assimilation system (NLDAS) fields. Canopy closure is estimated using MODIS LAI data (MOD15A2H) in combination with the Global Land Analysis and Discovery (GLAD) tree height dataset (Myneni et al., 2015; Potapov et al., 2020). LAI is downscaled from 500 m to 30 m using Global Tree height as a proxy as described in Appendix C.

When coarsening the land-cover data from 30 m to 90 m resolution, a pixel is classified as forested if the dominant landcover in the pixel is forest. Note however that there is subpixel scale variability in land cover and this heterogeneity can be spatially organized as shown in Fig.3. Table 1 provides a comprehensive summary of the datasets, raw and final resolution, sensors used to acquire the datasets and access links, as used in the SWE retrieval algorithm.

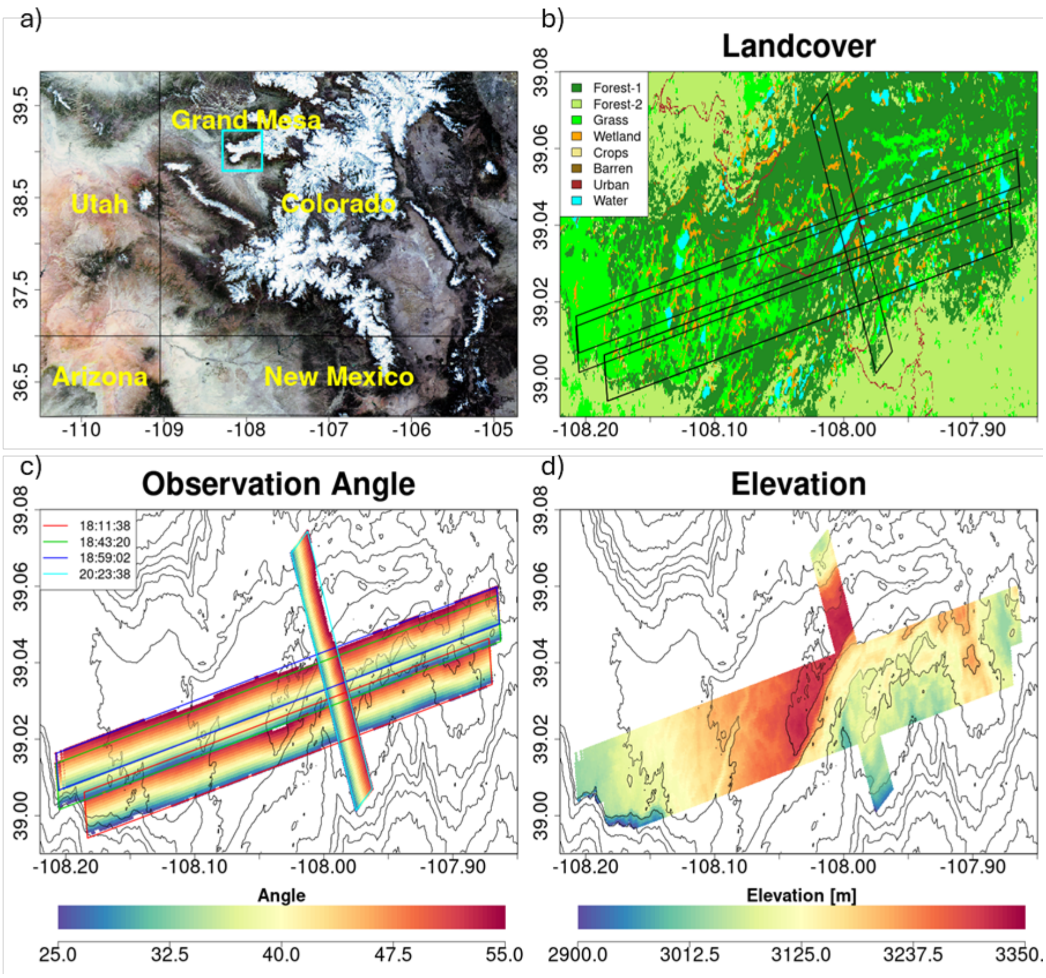

Figure 2 - Study area in Grand Mesa, Colorado. a) Location of Grand Mesa in Colorado, with historical Apr 1 SWE average as base map. b) Land cover of the study region. Forest-1 are needle leaf forests; Forest-2 are broadleaf forests. c) Paths of 4 SnowSAR SnowEx'17 flights on 21 Feb 2017, with true color image obtained from Landsat on 03/11/2017 as the base map d) Digital elevation map of the study region.

https://doi.org/10.5194/egusphere-2026-3588
Preprint. Discussion started: 4 August 2026

2.1 Atmospheric Forcing

Numerical Weather Prediction (NWP) data are used to provide atmospheric forcing and boundary conditions for the snow hydrology model. We utilize hourly forecasts from the High-Resolution Rapid Refresh (HRRR) model developed by the National Oceanic and Atmospheric Administration (NOAA), which assimilates observations at 3 km resolution (Benjamin et al., 2016). We modified the incoming shortwave and longwave radiation from HRRR using equation (A.1-A.2) for canopy shadow effects in forested areas. Canopy closure (C_c) is derived by downscaling the MODIS LAI dataset (500 m resolution) to 30 m, using tree height as a covariate (See Appendix A). Snowfall interception is calculated using equation (B1) and subtracted from the incoming precipitation, while the unloading of intercepted snow is subsequently added to the snowpack. The density of unloaded snow, which differs from fresh snow due to metamorphic processes, is calculated using equation (B7). Atmospheric forcing variables are linearly interpolated to match the 30-minute temporal resolution 90 m spatial resolution to be used in the model.

Table 1- Summary list of datasets used in the study.

Data	Source/ Sensor	Spatial Resolution		Temporal Resolution		Date Range	Relevant Link
		Initial	Final	Initial	Final		
Rainfall Temperature Air Pressure Incoming SW radiation Incoming Longwave radiation Wind speed Humidity	HRRR	3 km	90 m	1 hr	30 min	9/1/2016 - 2/25/2017	https://rapidrefresh.noaa.gov/hrrr/
Albedo	NLDAS	12.5 km	30 m	1 hr	30 min	9/1/2016- 2/25/2017	https://ldas.gsfc.nasa.gov/
Backscatter	SnowSAR – SnowEx'17	1 m	90 m	-	-	2/21/2017	https://nsidc.org/data/snex17_snowsar/versions/1
Landcover	NLCD	30 m	90 m	-	-	-	https://www.usgs.gov/centers/eros/science/national-land-cover-database
Snow Depth	LiDAR – SnowEx'17	3 m	90 m	-	-	2/25/2017	https://nsidc.org/data/aso_3m_sd/versions/1
SWE	Snowpit – SnowEx'17	-	-	-	-	2/20/2017- 2/24/2017	https://nsidc.org/data/snex17_snowpits/versions/1
LAI	MODIS	500 m	90 m	1 Day	1 Day	9/1/2016 - 2/25/2017	https://modis.gsfc.nasa.gov/data/dataprod/mod15.php
Tree Height	GLAD	30 m	90 m	-	-	9/1/2016 - 2/25/2017	https://glad.umd.edu/dataset/gedi

2.2 SnowSAR Backscatter

Airborne microwave backscatter measurements were acquired over Grand Mesa on 21 February 2017 during the NASA SnowEx campaign using the SnowSAR instrument, a dual-frequency (X- and Ku-band) synthetic aperture radar system (see Singh et al., 2024; Table 1). The data were collected at ~1 m resolution along six flightlines - two over steep, densely forested terrain and four over the plateau. Only the plateau flightlines are used in this study (Fig. 2, Fig. 3), corresponding to flight times between 18:00 and 21:00 GMT (12:00–15:00 MST).

https://doi.org/10.5194/egusphere-2026-3588
Preprint. Discussion started: 4 August 2026

SnowSAR data underwent rigorous quality control, including filtering based on aircraft attitude (e.g., turbulence-induced instability), beam incidence angle, antenna pattern, and signal-to-noise ratio (Reference). As established in prior analyses, only the co-polarized (HH and VV) backscatter measurements are retained for retrieval due to their consistent signal quality. Geolocation accuracy was validated using corner reflectors and prominent geographic features. Figure 2 shows the flight paths and the observation angles of the retrieved backscatter measurements. The original 1m SnowSAR data were aggregated to 30 m and to 90 m grids by averaging all valid observations within each pixel. Figure 3 shows the spatial distribution of open and forested pixels for all SnowSAR flights at 90 m resolution.

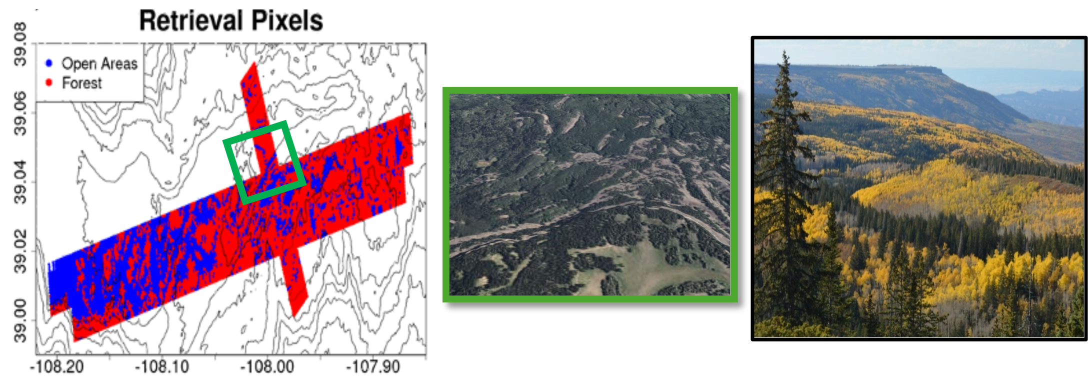

Figure 3 – Left panel: Spatial distribution of retrieved pixels at 90 m resolution differentiating between open (blue) and forested (red) areas along the flight lines. Singh et al. (2024) retrievals were for the open areas. Central panel: Spatial patterns of seasonal rocky open areas and wetlands embedded in evergreen forested areas (green box) that are not captured at 90 m resolution resulting in land-cover classification uncertainty. Source: Google Maps. Right panel: Mixed evergreen (pines) and deciduous (aspen) forest in the fall. Note some aspen trees have already lost their leaves. Source: https://adventr.co/2016/09/grand-mesa-fall-colors-2/

2.3 Validation Data

LiDAR Snow Depth: Airborne Snow Observatory (ASO) LiDAR measurements of snow depth at 3 m spatial resolution were acquired over Grand Mesa on 25 February 2017, four days after the SnowSAR flights (Painter et al., 2018). No significant snowfall or high-wind events occurred during this period, aside from a brief (~1 hour) rainfall event of approximately 3 mm on 24 February. The ASO LiDAR data are used to assess the spatial distribution of retrieved snow depths, characterizing snowpack heterogeneity, and to quantify absolute differences between retrievals and observations as estimates of local pixel-scale retrieval errors. The LiDAR snow depth data were aggregated to 90 m resolutions. Consistent with previous studies, LiDAR underestimation is more likely near forest edges due to partial occlusion and terrain effects (Deems et al, 2013; Jacobs et al., 2021). To mitigate the impact of measurement uncertainty LiDAR pixels with snow depths less than 20 cm are excluded from the evaluation. Additionally, high subgrid scale standard deviation of more than 0.3 typically found near the forest edges and highly heterogenous mixed pixels are removed from the final data (Singh et al., 2024).

Snowpit Dataset: Multiple snowpits excavated across Grand Mesa during the SnowEx'17 field campaign to obtain in situ measurements of snow water equivalent (SWE) (Table 1). While snowpit data along the SnowSAR flightlines on 21 February were limited, measurements collected between 20–24 February were included for evaluation. This assumes minimal changes in the snowpack over the four-day period, thus assuming that wind redistribution, sublimation and snowfall are negligible in the absence of snowfall. Although localized variability may exist, broader spatial patterns such as the characteristic west-to-east gradient in snow depth are expected to remain stable.

3. Methodology

https://doi.org/10.5194/egusphere-2026-3588
Preprint. Discussion started: 4 August 2026

The physical-statistical framework proposed by Singh et al. 2024 consists of using the Multilayer Snow Hydrology Model (MSHM) to inform prior distributions of snowpack physical parameters. The MSHM is coupled to a Radiative Transfer Model, MEMLS3&a (Proksch et al. 2015; Wiezmann and Mätzler, 1999) to simulate total backscatter at a given frequency and polarization. The Bayesian inference goal is to estimate optimal distributions of snowpack physical parameters by minimizing the difference between simulated and observed total backscatter at each pixel: that is, by maximizing the posterior probability of snowpack physical parameters conditional on the measurements and informed by the priors. This is achieved using a Monte Carlo Markov Chain (MCMC) iterative algorithm (Metropolis et all, 1953) following Pan et al. (2023). Instead of using an empirical soil model to estimate soil dielectric properties as in (Dobson et al., 2007; Mironov et al., 2009), Singh et al., 2024 implemented a sequence of two Bayesian retrieval steps taking advantage of backscatter measurements with different polarization: one for the ground parameters alone (soil moisture and surface roughness), and one for the snowpack. To extend the physical-statistical model to forested areas, a parameterization of vegetation backscatter is added to the RTM, and a third intermediate Bayesian retrieval step is added to estimate the vegetation parameters. The snow hydrology model was also modified to better simulate snowpack physics under the canopy.

Table 2 - Models, input variables, and corresponding outputs used in the SWE retrieval framework

Model	Input	Output	Reference
MSHM (Modified for Vegetation)	Rainfall Temperature Air Pressure Incoming shortwave radiation Incoming longwave radiation Wind speed Humidity Albedo LAI Based C_c	Snow Temperature Profile Soil Temperature Profile Snow Density Profile Snow Depth Layering Profile Liquid Water Content Profile Snow Correlation Length	MSHM Cao and Barros 2023
MEMLS + WCM	Snow Temperature Profile Soil Temperature Profile Snow Density Profile Snow Depth Layering Profile Snow Correlation Length Profile Cross polarization fraction Ground rms height Frozen Vegetation Water Content	Diffused Reflectivity Profile Specular Reflectivity Profile Total Backscatter Coefficient	MEMLS: Proksch et al., 2015 WCM: Bindlish and Barros, 2001
Informed Bayesian RTM for forested areas	Equivalent Snow Temperature Prior Equivalent Soil Temperature Prior Equivalent Snow Density Prior Equivalent Snow Depth Prior Correlation Length Cross polarization fraction Interpolated Ground rms height Interpolated Frozen Soil Moisture Frozen Vegetation Water Content Total Backscatter Coefficient Prior LAI Based C_c	Optimized – Snow Layer Depth Snow Density	Informed Bayesian RTM for Open areas: Singh et al., 2024

3.1 Parameterization of Vegetation Backscatter

Simulation of vegetation backscatter depends on factors such as vegetation type, leaf orientation and distribution, vegetation temperature, and water content. Vegetation backscatter models are typically categorized into three types: (i) empirical, (ii) semi-empirical, and (iii) theoretical. Empirical models, such as the Dubois model and machine

https://doi.org/10.5194/egusphere-2026-3588
Preprint. Discussion started: 4 August 2026

learning models, rely heavily on large, site-specific datasets to estimate radar backscatter (Dubois et al., 1995; Baghdadi et al., 2012; El Hajj et al., 2016; Mueller et al., 2022). As a result, these models are not well-suited for use in radiative transfer-based retrieval algorithms for general applications. Semiempirical models such as the Oh and the Water Cloud Model (WCM) integrate site specific parameters within a physical framework (Attema and Ulaby 1978; Bindlish and Barros 2000; Li and Wang 2018; Oh et al., 2022). In contrast, theoretical models like the Integral Equation Model (IEM) use detailed vegetation properties including canopy structure, water content, and biomass to simulate radar backscatter (Khabazan et al., 2013; Panciera et al., 2013). However, the extensive input requirements of these latter models limit their applicability in large-scale or operational retrievals, where such detailed vegetation characteristics and other ancillary data are often unavailable. These challenges highlight the need for scalable, physically grounded models that can balance complexity with data availability to improve vegetation correction in snowpack retrievals.

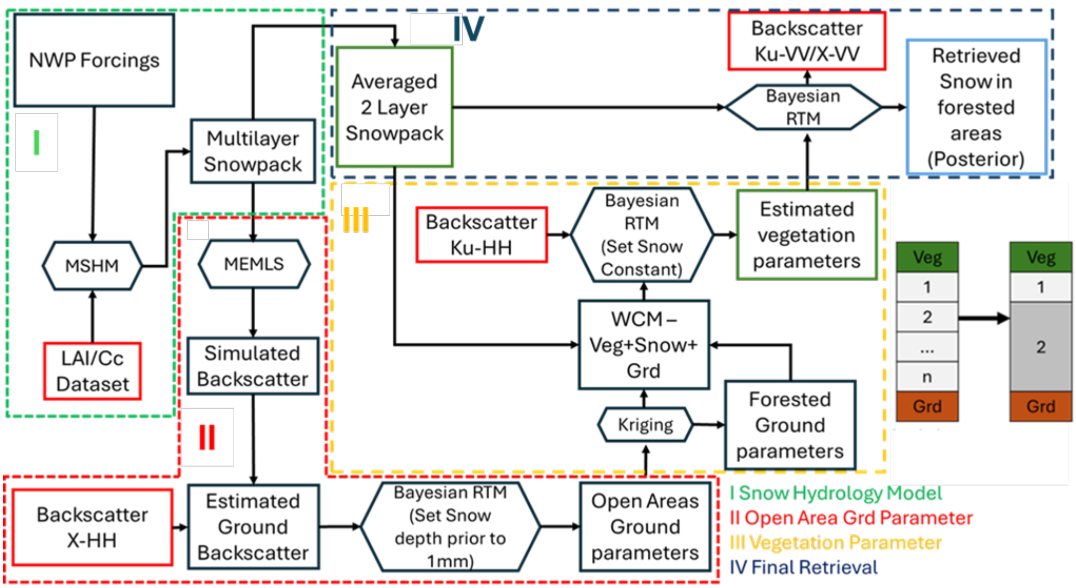

Figure 4- Methodology to determine SWE in forested environments. The workflow is divided into four main steps: (I) Snow Hydrology Model (green) - to simulate snow accumulation; (II) Open-Area Ground Parameterization (red) - to retrieve scattering and attenuation parameters for snow over in open areas; (III) Vegetation Parameterization (yellow) - to estimate vegetation-related parameters such as canopy transmissivity and vegetation water content; and (IV) Final Retrieval (blue) - integrates vegetation and ground contributions to estimate SWE within forested pixels. Step (I) retrieved parameters. The Bayesian framework is implemented sequentially where posterior parameter estimates from each stage are propagated as prior information for subsequent stages. Specifically, open-area ground parameters retrieved in Step II are used as priors for vegetation parameter estimation in Step III, and the posterior distributions of both vegetation and ground parameters are subsequently used as priors in the final SWE retrieval (Step IV), thereby reducing parameter uncertainty and ensuring physical consistency across the workflow.

The WCM combines transmissivity, vegetation backscatter and ground backscatter parameters to determine total backscatter from a vegetated pixel (Attem and Ulaby 1978; Bindlish and Barros 2000; Vermunt et al., 2022). Previous WCM applications have been directed at soil moisture retrievals from radar measurements. In a typical WCM application the vegetation backscatter is estimated using empirical relations based on ancillary data and or remote-sensing vegetation indices derived by optimizing frequency and polarization dependent parameters against observations (Bindlish and Barros 2001; Kumar et al., 2012; Park et al., 2019; Qin et al., 2024). Here, the WCM is adapted to represent vegetation effects in SAR measurements over snow covered forested areas.

The total backscatter σ_{tot} includes contributions of vegetation backscatter from the forest canopy σ_{veg} and the snowpack $\sigma_{vol+bkg}$ that combines volume backscatter from the snowpack σ_{vol} and backscatter from the snow-ground interface (background) propagated through the snowpack. transmitted by ththe canopy with transmissivity τ_{veg} (Figure 1):

$$\sigma_{total} = \sigma_{veg} + \tau_{veg}(\sigma_{vol+bkg}) \tag{1}$$

$$\sigma_{vol+bkg} = \sigma_{vol} + \tau_{vol}\sigma_{bkg} \tag{2}$$

$$\sigma_{veg} = AM_v cos\theta \tag{3}$$

where M_v is vegetation water content, and θ is the incidence angle. Equation (2) represents the total backscatter in open areas and can be estimated using the RTM given the snowpack physical properties.

The vegetation transmissivity varies exponentially with the vegetation water content

$$\tau_{veg} = e^{-2BM_v sec\theta} \tag{4}$$

Thus, the parameterization adds three additional physical parameters: M_v, A and B. These parameters vary from one pixel to another, and A and B are frequency and polarization dependent calibration parameters. Consequently, one intermediate Bayesian estimator is added to the physical-retrieval framework in Singh et al., 2024 to estimate prior distributions of vegetation parameters as described below.

3.2 Physical-Statistical Retrieval

The methodology comprises four steps: i) Determination of C_c and simulation of snowpack parameters using MSHM, ii) Determination of ground parameters, iii) Determination of vegetation parameters, and iv) Retrieval of snowpack parameters from SnowSAR backscatter. Figure 4 shows the flowchart for the proposed retrieval algorithm to retrieve the snowpack and vegetation parameters built on the Bayesian retrieval algorithm originally developed by Pan et al. (2023) and modified by Singh et al. (2024). The MSHM with forest shadow effect and interception parametrizations is used to simulate snowpack evolution since the beginning of the snow accumulation season for each pixel. For retrieval, the multilayered snowpack is transformed into a two-layered snowpack based on the relative change in the density profile criteria proposed by Singh et al. (2024). MEMLS is used to simulate snowpack and snow-ground backscatter, while the WCM is applied for vegetation backscatter. Table 2 provides the list of input and output variables associated with each model - MSHM, MEMLS-WCM, and the Bayesian RTM along with corresponding references.

3.2.1. Numerical simulation of snowpacks using MSHM (Step I)

The input datasets, including atmospheric forcing and remotely sensed variables were prepared and modified for integration into the modeling framework following Cao and Barros (2020). As previously discussed, canopy closure (C_c) was derived by downscaling the MODIS LAI product, removing zero values associated with open areas, and redistributing LAI values proportionally based on the GLAD tree height dataset. Incoming radiation and precipitation were adjusted using Eqs. (A1-B4). Specifically, incoming solar radiation was modified using canopy closure and transmissivity values obtained from literature, while precipitation was reduced based on interception calculated using the Hedstrom and Pomeroy (1998) model (HP98 hereafter). MSHM was further modified to incorporate intercepted snow unloading as an additional forcing input, with the corresponding snow density computed using Eqs. (B5-B7). The final processed datasets are used as inputs to inform and constrain the retrievals.

3.2.2 Determination of Ground parameters (Step II)

The ground parameters were initially estimated following the methodology described in Singh et al., (2024), by setting the snow depth at 1 mm and using X-band HH-polarized backscatter in open areas. The retrieved ground parameter values showed minimal spatial variability, with pixel-to-pixel changes not exceeding 1%, which allowed us to assume the validity of the First Law of Geography across different land cover classes. This justified the use of ordinary kriging to spatially interpolate background priors into the forested regions. Nevertheless, ground parameter values near forest edges appeared anomalously high due to significant residual errors in the simulated backscatter. To reduce the

https://doi.org/10.5194/egusphere-2026-3588
Preprint. Discussion started: 4 August 2026

influence of these outliers, we restricted the spatial interpolation to values within the 95% confidence interval, thereby improving the robustness and reliability of the estimated ground parameters.

3.2.3 Determination of vegetation parameters (Step III)

To establish background and vegetation priors, we used Ku-band HH-polarized backscatter while holding snowpack parameters constant and allowing vegetation and ground parameters to vary. This step completes the baseline initialization for subsequent SWE retrieval. Given that all vegetation parameters (*A*, *B* and *Mv*) in the Water Cloud Model (WCM) are unknown for each pixel, one parameter out of the three must be fixed to reach a unique solution. Note that in this study we rely on one-time measurements at each location as even in the case of overlapping pixels between adjacent SnowSAR flight lines there are significant differences in SAR geometry due to the low aircraft altitude. In the case of an operational satellite mission obtaining systematic measurements from long distances in Low Earth Orbit (LEO), it is possible to use the time-series backscatter measurements obtained at each location to infer (*A*, *B* and *Mv*) at longer timescales, and thus the parameter estimation problem would be highly simplified.

The apparent canopy architecture and water content will change principally due to interception of snowfall during the accumulation phase until the canopy structural storage capacity is exhausted, assuming weak winds and sublimation. Subsequent changes will be due to unloading and melting in the warm season, which are not considered here. As the intercepted snowfall has low values, maximum value of 0.1 mm (Figure C.1), we omitted the backscatter from interception in our simulation. An initial value of $A = 0.0014$ is assumed as a starting point for optimization following Bindlish and Barros (2001). Since the WCM was originally developed for unfrozen conditions and only one parameter was fixed, all retrieved values are considered effective parameters rather than fully physical. During the final retrieval (Step IV), ground surface roughness estimated in Step II was held constant due to its high sensitivity, while soil moisture was treated as an uncertain parameter and optimized. Vegetation water content, retrieved in Step III, was assumed to be constant across frequencies and polarizations (Table 5).

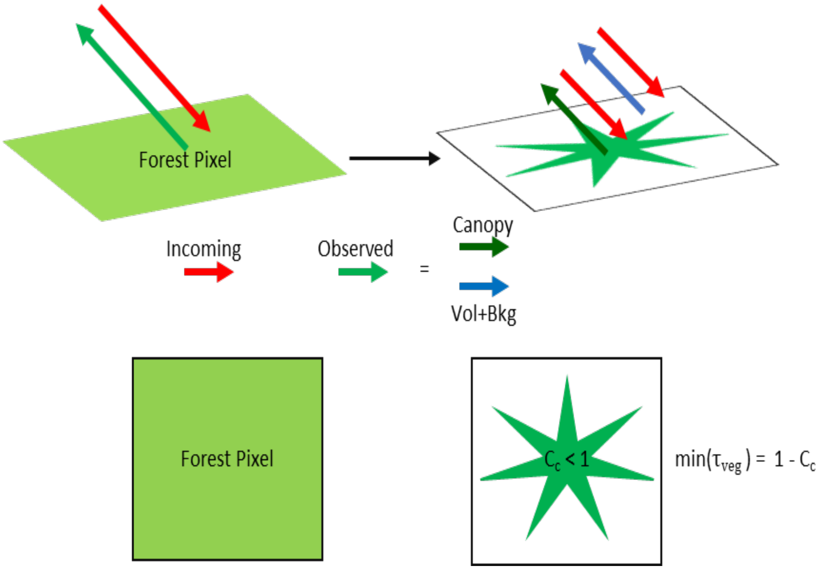

Figure 5 - Conceptual illustration of radiative partitioning and microwave backscatter contributions in a mixed forest pixel. The left panel shows total observed backscatter from a pixel labeled "forest" in the land cover dataset, comprising both canopy-covered and open areas. The top panel separates this pixel into fractional components: canopy and open. Canopy closure (C_c) determines the fraction of vegetation-influenced backscatter. Minimum transmissivity is constrained by $1-C_c$, while maximum vegetation backscatter is bounded by assuming total reflection. These constraints are used to derive physical limits for WCM parameters as outlined in Eqs. (1–3).

https://doi.org/10.5194/egusphere-2026-3588
Preprint. Discussion started: 4 August 2026

Figure 5 shows the partitioning of radiation in a mixed pixel identified as vegetation or forest using the landcover dataset. Under an idealized partitioning scenario assuming no other presence of any material except tree, the minimum transmissivity of vegetation within a mixed pixel is bounded by (1-C_c):

$$\min(\tau_{veg}) \quad = 1 - C_c \tag{5}$$

Therefore Eq. (4) can be expressed as,

$$1 - C_c = e^{-2BMv\sec\theta} \tag{6}$$

Keeping site specific A constant, we assume σ_{veg} depends linearly only on Mv (Eq. 3). Therefore, the maximum contribution by the vegetation backscatter to the observed backscatter (Eq. 1) is limited by the canopy closure:

$$\sigma_{obs} = \sigma_{veg} + (1 - C_c)\sigma_{vol+bkg} \tag{7}$$

The maximum value of the vegetation water content, Mv_{max} , can be expressed as

$$Mv_{max} = \frac{\sigma_{obs} - (1 - Cc)\sigma_{vol+bkg}}{A\cos\theta} \tag{8}$$

Similarly, in step IV of the retrieval algorithm (Figure 4), A and B are optimized while keeping Mv from step III constant, the maximum limits of the parameters are,

$$A_{max} = \frac{\sigma_{obs} - (1 - C_c)\sigma_{vol+bkg}}{Mv\cos\theta} \tag{9}$$

$$B_{max} = -\frac{\log(1 - C_c)\cos\theta}{2Mv} \tag{10}$$

These constraints provide a narrow and physically plausible range for the parameters improving the stability of the optimization scheme.

Table 3 - Ground parameter input mean, variance and range for the parameters. Frequency used to determine retrieve the parameter are mentioned in the Table. Alphanumeric subscript int – interpolated using open area parameters retrieved using Singh et al. (2024).

Background Parameters	**Frequency – Ku-HH**			
	Mean	**Variance**	**Range**	
			Min	**Max**
Effective Soil Moisture, Mvs	Mvs_{int}	$0.3\times Mvs_{int}$	0	1
Ground Roughness, *GndSig*	$GngSig_{int}$	$0.3\times GngSig_{int}$	0.0001	1

3.2.4. Retrieval of Snowpack Parameters (Step IV)

The multilayer snowpack predicted by the snow hydrology model (MSHM) is transformed into an equivalent two-layer snowpack by determining layers with maximum change in relative density following Singh et al. (2024). The standard deviation and value ranges for snowpack, background and vegetation priors used in the optimization are detailed in Tables 3–6. The final optimization simultaneously retrieves the following parameters: snow depth, snow density, snow correlation length, snow and soil temperature, frozen soil moisture, and WCM vegetation backscatter coefficients (A and B), using dual frequency X-VV and Ku-VV-backscatter. Detailed analysis of the vegetation parameters is presented in Appendix D. Figures D.1 and D.2 show the spatial maps of the mean of the posterior distributions of A and B for each frequency.

https://doi.org/10.5194/egusphere-2026-3588
Preprint. Discussion started: 4 August 2026

Table 5 -Vegetation parameter input mean, variance and range for the WCM parameters to optimize in Step II (Figure 4).

Veg Parameters	**Frequency – X, Ku Band VV Pol**			
	Mean	**Variance**	**Range**	
			Min	**Max**
A	$A_{avg} = \frac{A_{max} + A_{min}}{2}$	$0.3\times A_{avg}$	$0.1A_{max}$	$\frac{\sigma_{obs} - (1 - C_c)\sigma_{vol+grd}}{Mv\cos\theta}$
B	$B_{avg} = \frac{B_{max} + B_{min}}{2}$	$0.3\times B_{avg}$	$-\frac{\log(0.991)\cos\theta}{2Mv}$	$-\frac{\log(1 - C_c)\cos\theta}{2Mv}$

Table 6 - Bayesian RTM model input variance and range for the priors derived from MSHM multilayer snowpack properties. The alphanumerical subscript in the 2-layer snowpack retrievals denotes layer number: 1- bottom layer; 2- top layer; avg is the average of all MSHM multilayer parameter values in the corresponding 2-layer snowpack.

Snow + Background Parameters	**Frequency – X-VV and Ku-VV**			
	Variance, σ^2		**Range for each layer**	
	Bottom	**Top**	**Min**	**Max**
Snow Temp., Ts [^{O}C]	$0.3\times Ts_{1,avg}$	$0.3\times Ts_{2,avg}$	$1.3\times Ts_{min}$	$0.7\times Ts_{max}$
Snow Density, ρ [Kg/m^3]	$0.3\times \rho_{1,avg}$	$0.3\times \rho_{2,avg}$	$0.8\times \rho_{min}$	$1.2\times \rho_{max}$
Layer Snow Depth, DZ [m]	$0.1\times DZ_1$	$0.2\times DZ_2$	$0.2\times DZ$	$0.95\times DZ$
Correlation Length, l_{ex}	$0.2\times l_{ex,1,avg}$	$0.2\times l_{ex,2,avg}$	$l_{ex,min}$	$l_{ex,max}$

3.3 Evaluation of Retrievals

Point-scale validation was first conducted using independent SWE measurements from SnowEx'17 snow pits. For each pit, all SnowSAR pixels with centroids within a 100 m radius were identified, and the mean distance from the pit and the forest fraction within this buffered region were calculated using the reclassified land-cover dataset. Retrieval skill was quantified using mean absolute relative error (MARE). Successful retrievals were defined as pixels with local incidence angles between 30° and 50°, and relative residual backscatter (RRB) less than 30%.

https://doi.org/10.5194/egusphere-2026-3588
Preprint. Discussion started: 4 August 2026

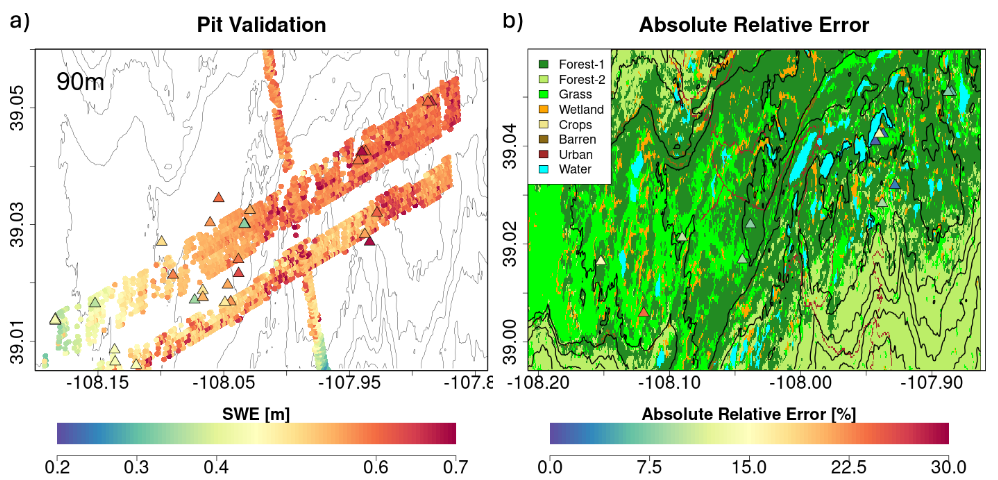

Figure 6- a) Comparison between retrieved SWE and pit observations. Successful retrievals are for pixels with local incidence angles in the 30º- 50º range and relative residual backscatter (RRB) of less than 30% for each of the four flights. The triangles mark pit locations and are colored according to SWE magnitude. b) Spatial distribution of pit locations (triangles) with at least 1 retrieved pixel within 90 m overlaying a land cover basemap. The triangles are colored according to absolute relative error magnitude. Note there are only three pixels with ARE greater than 10% and one pixel with ARE > 15%.

Table 7 - Evaluation of successful SWE retrievals at 90 m resolution against SWE at SnowEx'17 snow pits identified by their ID and coordinates (X,Y). The centroids of the N pixels used in the evaluation are within 100 m of the snow pits. The standard deviation (SD), average distance from all pits (ADP), and average pit forest fraction (APFF) are calculated for the circle with 100 m radius around each.

X	Y	Swe-Pit [m]	Swe-Ret [m]	SD (Ret)	MARE [%]	N pixels	ADP [m]	APFF	Date	Pit ID
-107.94	39.04	0.60	0.59	0.008	2	6	10	0.97	2/21/2017	Pit71E
-107.93	39.03	0.61	0.59	0.047	3	3	27	0.21	2/21/2017	Pit74E
-108.15	39.02	0.36	0.41	0.008	14	4	62	0.64	2/22/2017	Pit26W
-108.12	39.01	0.44	0.55	-	25	1	71	0.39	2/22/2017	Pit32S
-108.09	39.02	0.58	0.52	0.013	10	3	14	0.5	2/22/2017	Pit38E
-108.04	39.02	0.57	0.52	0.001	9	2	45	0.58	2/22/2017	Pit63E
-108.04	39.02	0.59	0.54	0.013	8	2	3	0.58	2/22/2017	Pit66N
-107.89	39.05	0.66	0.62	0.01	6	2	30	0.64	2/22/2017	Pit92E
-107.89	39.05	0.60	0.65	-	8	1	73	0.63	2/22/2017	Pit92W
-107.94	39.04	0.59	0.59	0.016	0	6	6	0.97	2/23/2017	Pit69N
-107.94	39.04	0.69	0.59	0.013	14	3	14	0.97	2/23/2017	Pit71W
-107.94	39.03	0.56	0.61	-	9	1	22	0.74	2/23/2017	Pit72S

Next, the retrieved snow depth is compared against collocated LiDAR snow depth observations averaged to 90m. LiDAR pixels with subgrid scale snow depth standard deviation greater than 0.3 m were removed due to high uncertainty in the estimates. Metrics such as the root mean square difference (RMSD) and the Bhattacharya coefficient

https://doi.org/10.5194/egusphere-2026-3588
Preprint. Discussion started: 4 August 2026

(BC) were used for assessing performance of the retrieved snow depth against LiDAR snow depth. BC is calculated as follows,

$$BC = \sum_{i=1}^{N} \sqrt{p_1(i)p_2(i)} \tag{11}$$

Here p_1 and p_2 represent the normalized probability distributions of snow depth for the retrieved and reference (LiDAR) datasets, computed using 200 bins over a 3 m depth range. The BC quantifies the degree of overlap between these two distributions, where values close to 1 indicate strong similarity and good agreement (Bhattacharya 1943). To evaluate the impact of spatial averaging on retrieval accuracy, we also performed retrievals at the 30 m resolution for the shorter flight running perpendicular to the plateau. This allowed for a direct comparison with 30 m LiDAR data to assess potential errors introduced by upscaling of categorical landcover datasets. The methodology for generating and comparing high-resolution retrievals is the same independently of spatial resolution. Because LiDAR snow depth itself is a derived product with well documented uncertainties as discussed earlier, we report retrieval-LiDAR differences rather than errors properly. Therefore, in this case we introduce the absolute relative difference (ARD) between retrieval and LiDAR with respect to LiDAR observations.

4. Results

The mean values of the posterior distributions in Step IV are used for assessing retrieval performance against snowpit measurements and LiDAR snow depth estimates. Figure 6 shows the spatial distribution of snow depth retrievals for all 4 flights and pit observations for dates between 21-23 Feb. Note the agreement between the increasing snow depth from west to east consistent with the pit dataset in Fig. 6a. The map of absolute relative errors (ARE) in Fig. 6b shows small values (< 15%) except for the one pit on the edge of the plateau where the terrain slope is very steep. To evaluate the retrievals against point-scale snow pit measurements and use the maximum number of pits, all forested pixels within 100 m of the pits were considered. Table 7 shows the summary evaluation of retrieved SWE against SWE from snow pit observations. The overall RMSE is 0.033 m, which is 8% of maximum SWE. Pit32S with large mean distance from the retrieved flight pixels and with low forest fractions (forest edge) shows high MARE of 25%.

Figures 7 and 8 show the heatmaps of LiDAR snow depth against MSHM priors and SnowSAR retrieved snow depth, respectively. Histograms of the results with bin resolution of 0.015 m are shown on Fig. 9. The MSHM predicted priors do not capture the spatial variability for deeper snowpacks. This is expected due to underestimation of snowfall, wind redistribution, and other sources of uncertainty in operational forecasts (Cao and Barros, 2023). By contrast, the retrieved SnowSAR snow depths significantly improved the results both in terms of the range of snow depth and the SD of the distribution along the flight paths, with improved BC metric relative to the MSHM indicating that the spatial patterns of retrieved snow depth are in better agreement with the LiDAR.

Table 8 provides a summary for the intercomparison among the three snow depth datasets. The LiDAR snow depth in the forest pixels varies within a narrow range of snow depths (1.5-1.75 m), and there is a good agreement between the MSHM and the LiDAR snow depths. The performance of the retrieval algorithm deteriorates for the fourth shorter flight at 20:23:38 UTC as illustrated by the misalignment of the histograms in the bottom-right panel in Fig. 9 and the lowest BC metric in Table 8. The heatmaps and the snow depth histograms (Fig. 9) show a small number of outliers in the retrieved backscatter retrievals with large standard deviation and increased RMSD, biasing the metrics. Informed Bayesian retrievals show improvement in both the standard deviation and BC for all flights.

https://doi.org/10.5194/egusphere-2026-3588
Preprint. Discussion started: 4 August 2026

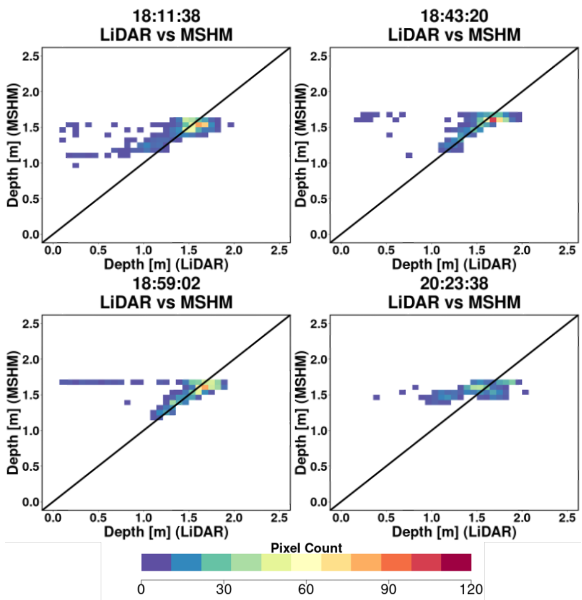

Figure 7 – Heatmaps of LiDAR versus MSHM predicted snow depth used as priors for each SnowSAR flight at 90 m resolution for overlapping forest pixels only. Flight times are in UTC.

338

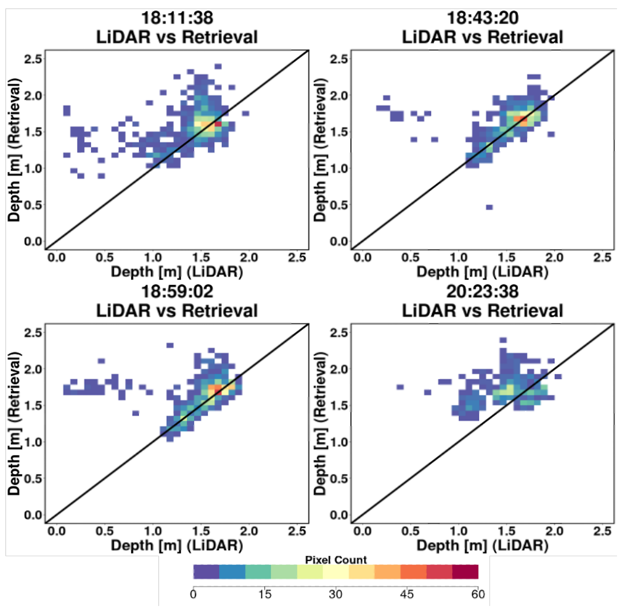

Figure 8 – a) Heatmaps of LiDAR snow depth versus successful snow depth retrievals at 90 m resolution for forest pixels only. Successful retrievals are for pixels with local SnowSAR incidence angles in the 30º- 50º range and relative residual backscatter (RRB) of less than 30%. Flight times are in UTC.

https://doi.org/10.5194/egusphere-2026-3588
Preprint. Discussion started: 4 August 2026

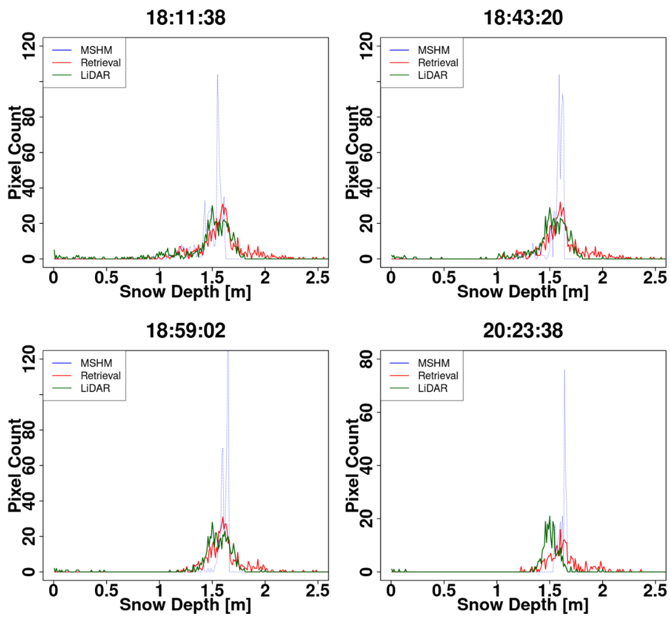

Figure 9- Histograms of snow depth predicted by MSHM used as priors, estimated from LiDAR measurements, and for successful SnowSAR retrievals at 90 m using a 2- layer snowpack. The total number of pixels for each snow depth product is the same. Successful retrievals are for pixels with local incidence angles in the 30°- 50° range and relative residual backscatter (RRB) of less than 30% for each of the four flights. Pixels with subgrid scale variability corresponding to standard deviation of less than 0.3 m for the upscaled 90 m LiDAR pixel are not included. Flight times are in UTC.

https://doi.org/10.5194/egusphere-2026-3588
Preprint. Discussion started: 4 August 2026

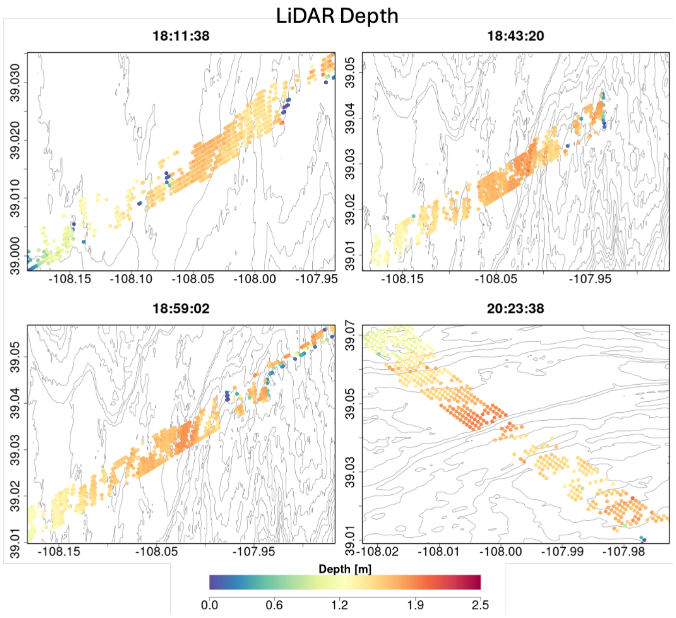

Figure 10 - Spatial distribution of LiDAR snow depth for forested areas with subgrid-scale standard deviation (SSD) of less than 0.3 m at 90 m resolution. Flight times are in UTC.

Examination of the spatial maps of LiDAR (Fig. 10) and retrieved snow depth (Fig. 11) and absolute relative difference with respect to LiDAR snow depth (Fig. 12) enables identification of potential error sources. In the first three flights LiDAR estimates along the edges of open areas are attributed to upscaling errors in land cover category, which is the mixed pixel artifact. In the final flight (20:23:38), large errors are present on the northernmost slope and in the highly heterogeneous areas surrounding small ponds. Because landcover is upscaled using nearest neighbor interpolation, areas with contrasting land-cover types and thus dielectric heterogeneity contain signal from non-forest areas thus introducing errors.

Table 8 - Summary of snow depth statistics and error metrics at 90 m resolution: estimates from LiDAR measurements (LiD), MSHM predictions, and successful SnowSAR retrievals (Ret) for forested pixels and subgrid-scale standard deviations of less than 0.3 m for the upscaled LiDAR pixel (Singh et al., 2024). BC – Bhattacharya coefficient (Eq. 15). Successful retrievals are for pixels with local incidence angles in the 30º- 50º range and relative residual backscatter (RRB) of less than 30% for each of the four flights.

Flight [UTC]	Mean [m]			Standard Deviation [SD]			BC		RMSD	
	Retrieval	MSHM	LiDAR	Retrieval	MSHM	LiDAR	Ret-LiD	MSHM-LiD	Ret-LiD	MSHM-LiD
18:11:38	1.59	1.50	1.46	0.22	0.10	0.30	0.87	0.76	0.15	0.06
18:43:20	1.62	1.55	1.56	0.20	0.12	0.24	0.94	0.70	0.06	0.01
18:59:02	1.64	1.55	1.53	0.20	0.12	0.30	0.89	0.78	0.11	0.03
20:23:38	1.71	1.58	1.51	0.20	0.08	0.27	0.78	0.68	0.2	0.07

https://doi.org/10.5194/egusphere-2026-3588
Preprint. Discussion started: 4 August 2026

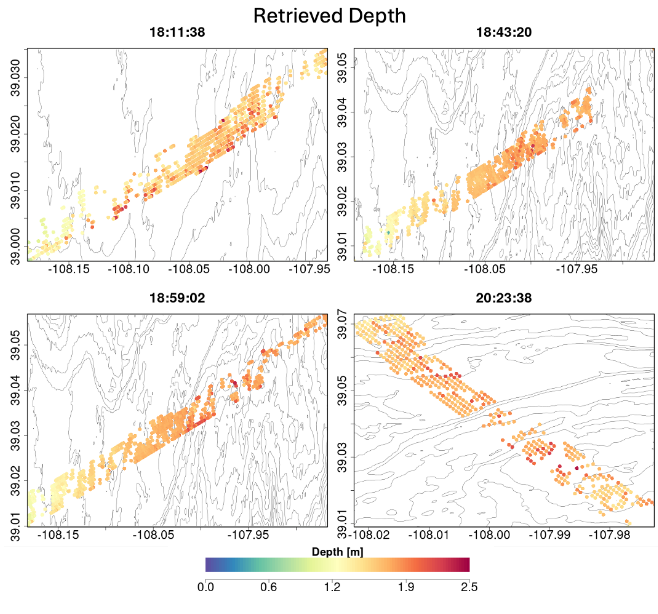

Figure 11 - Spatial distribution of snow depth SnowSAR retrievals at 90 m resolution for forested areas and for pixels with subgrid-scale standard deviation (SSD) of less than 0.3 m for the upscaled collocated LiDAR pixel. Flight times are in UTC.

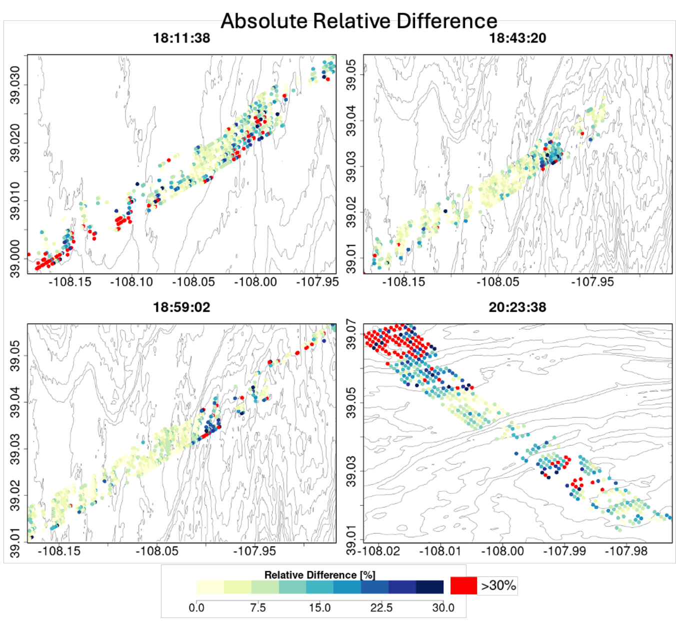

Figure 12- Absolute relative depth differences between snow depth from SnowSAR retrievals and LiDAR in Figures 10 and 11. The high values are either along the edges of the forest and nonforest land cover classes or in the mixed forest-pond-wetland pixels, especially on the slopes in the northern edge of the plateau where subgrid scale variability, and therefore uncertainty is high (see Fig.3b). This is also the region where LiDAR underestimation errors are expected to be higher (Deems et al., 2013). Flight times are in UTC.

https://doi.org/10.5194/egusphere-2026-3588
Preprint. Discussion started: 4 August 2026

As discussed in Section 3.5, to assess the errors introduced by the upscaling of categorical datasets such as forest cover and lake fraction, the subgrid-scale fraction of forest and lake were calculated for each pixel. Figure 13 shows the spatial distribution of forest fraction (top row), water fraction (bottom row), and the corresponding canopy closure within a 90 m pixel (mid row). Most forest pixels have forest fractions greater than 0.8 and lake fractions are zero. However, there are pixels at the edge of wetlands and open areas where the forest fraction is below 0.5. These pixels, even though classified as forest, have high subgrid scale variability. The canopy closure maps show values close to zero in areas where deciduous trees are dominant, and the LAI is near zero in winter. Nevertheless, in areas where there are evergreen trees (mostly pines) mixed with deciduous trees (Aspen) as shown in Fig. 3 (central panel), then the canopy closure parameter is much higher and these pixels along with pixels with lower forest fraction (below 0.8) at the edge of wetlands are the pixels with the largest absolute differences between retrieved snow depth and LiDAR snow depth for the flight at 20:23:38 UTC . For flights at 18:11:30 UTC and 18:43:20 UTC, regions exhibiting larger retrieval errors are in areas of high topographic variability, particularly along slope edges. In mixed forest pixels and pixels with high frozen lake fractions, biases in the backscatter signal due to mixed pixel effects propagate to the final SWE retrievals. Additional errors may arise from LiDAR underestimation of snow depth in sloped or densely forested areas as shown by Jacobs et al. (2021) and May et al. (2025). Jacobs et al. (2021) reported up to a 75% reduction in LiDAR point cloud density under dense canopy, leading to significant underestimation. Errors over steep terrain are further compounded by irregular ground point spacing, resulting in large interpolation errors (Deems et al., 2013). Therefore, quantitative evaluation of the SnowSAR retrievals against LiDAR-based estimates in such conditions, especially in the fourth flight (20:23:38), is impacted by these errors. Additionally, biases may also stem from the coarse resolution of atmospheric forcing datasets, such as HRRR precipitation (Cao and Barros 2023), which may not capture microclimatic variations along forested slopes and thus introduce larger uncertainty in the priors (English et al., 2021; James et al., 2022).

Beyond the empirical nature of the parameterization of C_c, uncertainties in MODIS-derived LAI may also affect retrieval accuracy (Peng et al., 2024). Finally, potential instrument-related biases, including calibration and viewing geometry effects, remain a critical area for future research. Nevertheless, we highlight the robust retrieval success for pixels with forest fraction greater than 70%, meeting desired Decadal Survey requirements (NASEM, 2018).

To illustrate the errors introduced due to upscaling of the land-cover categories, the retrievals were repeated at 30 m resolution for the shorter SnowSAR flight (20:23:38). Figure 14 shows a comparison between the 30 m SnowSAR retrievals and the LiDAR data at the same resolution. The RMSD for the 30 m for retrieval compared to LiDAR is 0.2m (compared to 0.33 m for 90 m retrievals) and the BC is 0.87 (0.78 for 90 m).The 30 m retrievals show improved agreement with LiDAR in terms of both mean and variance, and the areal extent of large relative errors (> 30%) is significantly smaller than at 90 m resolution. On the northern edge of the flight, where the evergreen forest fraction is near unity even though there is high heterogeneity in land cover (see Fig. 3, right panel), the areas where large absolute relative differences persist at 30m may be an indication of the bias in LiDAR estimates as discussed above, and not attributable to the retrievals. Additional analysis is imperative to eliminate the ambiguities needed to quantify the uncertainty both the SnowSAR backscatter measurements and LiDAR-based snow depth estimates in complex terrain. Nevertheless, these robust results indicate that it is possible to achieve low error retrievals in forest areas and in steep terrain at high spatial resolution by reducing heterogeneity errors.

https://doi.org/10.5194/egusphere-2026-3588
Preprint. Discussion started: 4 August 2026

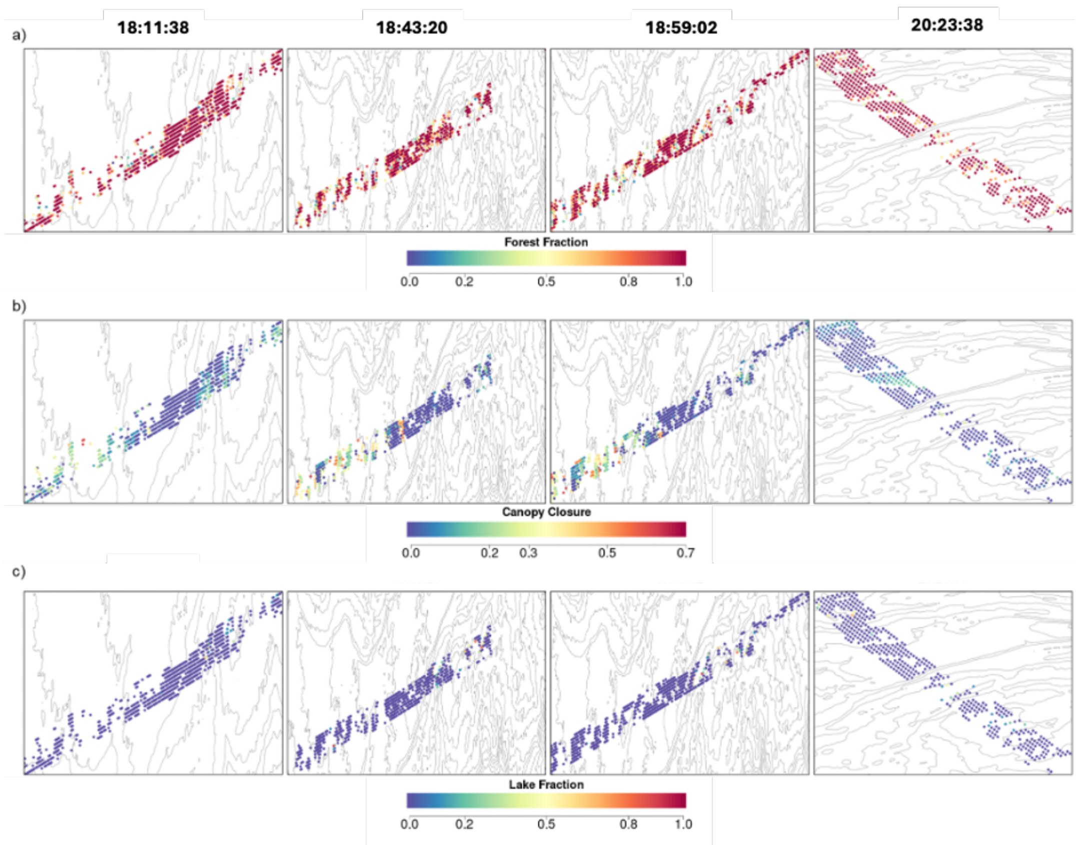

Figure 13 – Subgrid-scale variability at 30m that impacts retrieval uncertainty at 90 m: a) standardized forest fraction for a 90 m pixel using the 30 m land cover dataset; b) Canopy closure; c) standardized lake fraction for a 90 m pixel using the 30 m land cover dataset. Difference between frozen water and snow dielectric properties may introduce a bias in the final retrievals. Higher canopy closure values indicate the present of evergreen trees mixed with frozen wetlands and open areas. Flight Times are in UTC.

5. Conclusion

A Bayesian coupled atmosphere-statistical framework, building on prior studies, was used to retrieve snow water equivalent (SWE) from airborne X- and Ku-band radar observations in the presence of trees. The approach produced consistent and reliable results for four SnowSAR flightlines over the forested areas in Grand Mesa, Colorado. Prior estimates of snowpack properties were generated using a multilayer snow hydrology model (MSHM) driven by atmospheric forcing from operational numerical weather prediction (NWP) forecasts and analyses. MSHM is modified to account for forest canopy shadow and interception effects. The multilayered snowpack was averaged to two layers to reduce the number of parameters to be optimized as in Singh et al. (2024). Retrievals were conducted independently for each 90 m pixel along SnowSAR flight tracks using VV-polarized backscatter, and constrained by prior distributions of snow, background and vegetation parameters derived from MSHM, MEMLS and the Water Cloud Model (WCM) to parameterize vegetation, respectively.

https://doi.org/10.5194/egusphere-2026-3588
Preprint. Discussion started: 4 August 2026

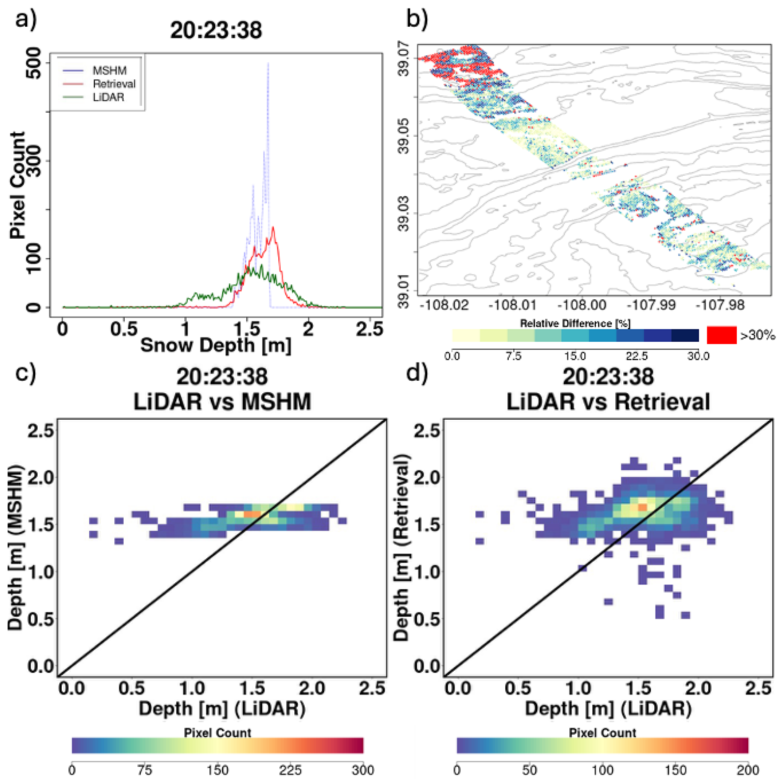

Figure 14- Comparison of 30 m SnowSAR retrievals and LiDAR snow depth for the 20:23:38 flight path. a) Retrieved snow depth at 30 m resolution. b) Absolute residual between SnowSAR retrievals and LiDAR snow depth. c) LiDAR snow depth at 30 m resolution and d) retrieved snow depth at 30 m. While the 30 m retrievals better capture mean and variance compared to coarser resolution retrievals at 90m, large residuals persist along the northern slope of the plateau due to terrain complexity and land cover heterogeneity (high lake faction). Flight times are in UTC.

A 30% threshold for relative residual backscatter was selected as a balance between physical quality and data retention. As shown in Appendix Figure E.1, RBB for most pixels is below 5%, however SnowSAR observations at 90 m resolution show elevated variability near forest edges (where most SnowEx pits are located), especially at Ku-band. Stricter limits would remove these physically meaningful signals and reduce spatial coverage. Therefore, the 30% criterion preserves continuity across snow–vegetation transitions and lan-cover boundaries while remaining consistent with physical expectations. Note that the need to constrain the incidence angle range to 30º-50º only arises because of the viewing geometry of the low altitude airborne measurements and it would go away for satellite-based SAR operations.

The mean values of the posterior distributions of retrieved snow depth were evaluated against collocated airborne LiDAR and snowpit SWE and snow depth measurements collected during the SnowEx'17 campaign, with validation restricted to pixels with centroids within 100 m of pit locations. The retrievals show strong agreement with pit observations, achieving an RMSE of 0.033 m, or approximately 8% of the maximum SWE measured. Comparisons with ASO LiDAR snow depth estimates confirm that the SnowSAR retrievals improve the spatial distribution of snow depth and distribution of snowpack structure, particularly in regions with deeper snow accumulation.

Errors and uncertainty in retrievals were spatially associated with heterogeneous landform and landcover. Particularly, large errors are observed near forest edges and steep slopes due to subpixel variability in elevation, forest fraction, and water presence. Consequently, validation performance in the fourth flight was limited due to increased terrain-

https://doi.org/10.5194/egusphere-2026-3588
Preprint. Discussion started: 4 August 2026

induced noise and fewer valid pixels. Additional uncertainty arises from LiDAR underestimation in dense canopies, coarse resolution of NWP weather forcing especially precipitation, and empirical uncertainties in MODIS LAI-derived canopy closure. These sources of uncertainty highlight the importance of improving subgrid-scale land cover characterization, and spatial resolution of ancillary data in future applications. Specifically, errors in canopy closure estimates can be reduced by leveraging repeated (time-series) observations from satellite-based backscatter measurements with short revisit times. Nevertheless, robust retrievals were achieved for pixels with forest fraction greater than 70%, meeting desired Decadal Survey requirements (NASEM, 2018).

This study demonstrates the viability of a dual-frequency, physically informed Bayesian retrieval framework for SWE estimation in complex forested landscapes. With continued advances in high-resolution SAR observations and global atmospheric reanalysis products, the methodology is extensible to large-scale operational applications and is particularly well suited for satellite-based snow monitoring missions.

Appendix

A. Representing Canopy Closure in MSHM

In addition to scattering, vegetation contributes to attenuation of solar radiation via absorption in the canopyin forested environments (Hardy et al., 2004; Wang et al., 2007; Essery et al., 2008). Most canopy radiative transfer schemes parameterize transmissivity (τ) using the Beer–Lambert law or two-stream approaches (Myneni et al., 1989; Sellers 1985; Sellers 1987), quantifying the fraction of radiation that penetrates the canopy after interacting with foliage through absorption and scattering. However, transmissivity alone does not capture the spatial variability in canopy density. During winter, deciduous trees lose their leaves, leading to substantial reductions in leaf area index (LAI) and canopy closure (Wang et al., 2016).

Because the degree of attenuation depends not only on the optical properties of the canopy but also on the fraction of sky obscured by vegetation, incorporating canopy closure (C_c) into the radiation transmissivity formulation is essential for accurately modifying the radiation incident upon the snowpack to account for shading and attenuation effects. The net downward flux of radiation reaching the snow surface beneath a canopy can be expressed as the sum of two components: (i) radiation transmitted directly through the open sky fraction ($1-C_c$), and (ii) radiation attenuated as it goes through the canopy. This leads to the following expressions for shortwave and longwave radiation beneath the canopy:

$$SW_{corr} = (1 - C_c)SW + \tau_{sw} C_c SW \qquad (A.1)$$

$$LW_{corr} = (1 - C_c)LW + C_c\left(\tau_{lw} LW + \kappa \epsilon_v T_{veg}^4\right) \qquad (A.2)$$

Here, the first term in each equation represents the fraction of radiation that reaches the snowpack directly through canopy openings, while the second term accounts for radiation transmitted through and emitted by the canopy layer. Assuming full-canopy conditions with minimal canopy gap fractions, the transmissivity terms (τ_{sw} and τ_{lw}) reflect the effective attenuation within dense forest stands with large observed canopy closure. Specifically, shortwave transmissivity (τ_{sw}) for conifer trees (Hardy et al. 2004) and decidous trees (Hardy et al., 1998); Longwave transmissivity (τ_{lw}) is derived from Asner et al. (1998) and longwave emissivity (ϵ_v) is obtained from Engineering Toolbox (2003).

A generalized model for remotely estimating canopy closure remains unavailable. Canopy closure (C_c) has been estimated empirically from field observations that relate measurable structural and spectral properties such as leaf area index (LAI), stand density, and gap fraction to closure. These empirical approaches are developed for specific canopy types and often rely on vegetation reflectance–based parameters as a proxy for closure. For example, Pomeroy et al. (2002) proposed an empirical parameterization canopy closure of conifer trees to Leaf Area Index (LAI):

$$C_c = 0.29 \log(LAI) + 0.55 \qquad (A.3)$$

The Leaf Area Index (LAI) is estimated from satellite-based surface reflectance, and thus there is a spatial resolution limitation tied to the reflectance data. Rasmus et al. (2013) showed that while the empirical relationship between LAI

https://doi.org/10.5194/egusphere-2026-3588
Preprint. Discussion started: 4 August 2026

and canopy closure in Eq. (A.3) works well for uniform forest stands with similar tree density and structure, its accuracy decreases in heterogeneous forests where canopy gaps and sub-canopy light conditions vary greatly. These uncertainties propagated into snow models, affect snowmelt timing and energy balance, particularly during the ablation period, and must be carefully assessed, particularly when applying the model across diverse forest types at varying spatial resolutions. Therefore, improvements in canopy structure estimation will be essential for enhancing the accuracy of snowpack retrievals in forested pixels. Bindlish and Barros (2001) introduced parameter dependence on vegetation architecture to distinguish between distinct types of crops in their application of the WCM parameterization. Given time-series of measurements such as those available from satellite missions revisits, it is possible to introduce such dependencies for forests with mixed tree species as the repeated measurements enable pixel (site specific) parameter estimation. In the absence of field measurements given the limited number of overlapping SnowSAR flights for Grand Mesa, and the lack of alternative parameterizations for different tree species and tree architectures, the Pomeroy et al. (2002) approach is adopted here. Both the field site in Pomeroy et al. (2002) and Grand Mesa is conifer-dominated, snow-bearing forests with similar canopy architecture and cold continental climates, and thus Eq. (A.3) provides a reasonable approximation of canopy closure for this study. A full analysis of uncertainty propagation has not been conducted.

B. Precipitation and Interception

Precipitation within forested environments should be modified according to interception efficiency of the overlying canopy. Fresh precipitation is reduced due to interception of snowfall in the canopy. High density is added to the snowpack due to unloading of intercepted snowfall. Multiple empirical models have been developed to determine interception in boreal forests (Hedstrom and Pomeroy 1998; Lundquist et al., 2021; Helbig et al., 2020). Tree architecture and stand density and diversity of tree species all impact interception. Stork et al. (2002) installed lysimeters to measure the mass balance on and around four trees and estimated a factor of 0.6 for interception. Hedstorm and Pomeroy (1998) derived a semi-empirical interception model fitting field measurements that is widely used:

$$I_{max} = 6.3LAI\left(0.27 + \frac{46}{\rho}\right) \quad (B.1)$$

$$dI_i = 0.68(I_{max} - I_{i-1})\left(1 - e^{-\frac{P_i C_c}{I_{max}}}\right) \quad (B.2)$$

$$P_{i,corr} = P_i - dI_i \quad (B.3)$$

$$I_i = I_{i-1} + dI_i - f_u - f_m \quad (B.4)$$

Here I_{max} is the maximum canopy interception; P_i is the snowfall and ρ is fresh snow density that is set as 30 kg/m^3 in the model (Singh and Barros 2024; Cao and Barros 2023); f_u and f_m are wind and melt unloading rates, respectively. Wind unloading can be quantified following Roesch et al. (2001):

$$fu = 0.0231W \quad (B.5)$$

where W is the average wind speed in ms^{-1}. Melt unloading and sublimation of intercepted snow are not considered in accumulation season simulations presented here. The unloaded snow is added to the snowpack in MSHM. The density of unloaded snow is estimated following Bouchard et al. (2022):

$$\rho_{s,int} = \rho_{fr} + (\rho_{max} - \rho_{fr})\left(1 - e^{-\frac{a_{s,int}}{\tau}}\right) \quad (B.6)$$

Here $\rho_{s,int}$ is the density of intercepted snow, ρ_{fr} is density of fresh snow taken as 30 kg/m^3. τ is an independent parameter such that $\rho_{s,int}$ reaches 99% of the maximum density of intercepted snow, $a_{s,int}$ within 30 days. If new snow is intercepted within 30 days, $a_{s,int}$ changes to,

$$a_{s,int} = a_{s,int}\left(1 - \frac{\Delta I}{I + \Delta I \Delta t}\right) \quad (B.7)$$

https://doi.org/10.5194/egusphere-2026-3588
Preprint. Discussion started: 4 August 2026

where Δt is computational period, 30 min in our case. Note that these empirical parameterizations of interception are site specific and their transferability has not been rigorously assessed to quantify uncertainty. Parameters such as interception efficiency and unloading coefficients are calibrated at point scale and may not generalize well to entire forest stands and larger spatial scales, limiting the robustness of SWE estimates in heterogeneous forested environments. Key sources to uncertainty include variability in canopy structure across forest types, inaccurate or generalized LAI and canopy closure inputs, errors in estimating wind speed at canopy level; simplifications in unloading dynamics, and uncertainty in fresh snow density, which may vary significantly with meteorological conditions.

C. Determination of high-resolution Canopy Closure

Leaf Area Index (LAI) values derived from MODIS (MOD15A2H) at 500 m resolution were downscaled to 90 m to support high-resolution retrievals. MOD15A2H provides both the mean and standard deviation of LAI per pixel. Figure A.1 illustrates the conceptual steps taken to estimate canopy closure (*C_c*) for a given pixel. For each 500 m pixel, subgrid (30 m) non-forest pixels were identified and assigned to a LAI value of zero. The forest-only LAI was then estimated by,

$$LAI_{forest} = LAI.\frac{N_{all}}{N_{forest}} \qquad (C..1)$$

Here N_{all} is all subgrid 30 m pixels, N_{forest} is the number of forest pixels and LAI is leaf area index of the mixed pixel. The adjusted standard deviation, after excluding non-forest contributions, was calculated as,

$$\sigma_{forest} = \sqrt{\frac{\sigma_{all}^2 . N_{all} - LAI^2 . N_{open}}{N_{forest} - 1}} \qquad (C.2)$$

Here σ_{all} is the original standard deviation of LAI for the mixed pixel and N_{open} is the number of open (non-forest) pixels. To spatially redistribute LAI across the 30 m forested subpixels, a normal distribution with the updated mean and standard deviation was sampled, using tree height as a covariate. The minimum and maximum bounds were defined as:

$$LAI_{min} = LAI_{forest} - 3\sigma_{forest} \qquad (C.3)$$

$$LAI_{max} = LAI_{forest} + 3\sigma_{forest} \qquad (C.4)$$

Previous studies have reported a positive relationship between canopy height and LAI across forest types, indicating that taller vegetation supports greater leaf area (Yuan et al., 2013; Urrego et al., 2021). This relationship provides a physical basis for using vegetation height as a covariate in redistributing LAI within mixed pixels. Therefore, the final downscaled LAI for each 30 m pixel was assigned based on the local vegetation height (*VH*) using a linear interpolation:

$$LAI_{30m} = LAI_{min} + \left(\frac{VH - VH_{min}}{VH_{max} - VH_{min}}\right) \times (LAI_{max} - LAI_{min}) \qquad (C.5)$$

This approach preserves subgrid variability and accounts for canopy structure in estimating canopy closure, a critical input for SWE retrievals in forested environments.

https://doi.org/10.5194/egusphere-2026-3588
Preprint. Discussion started: 4 August 2026

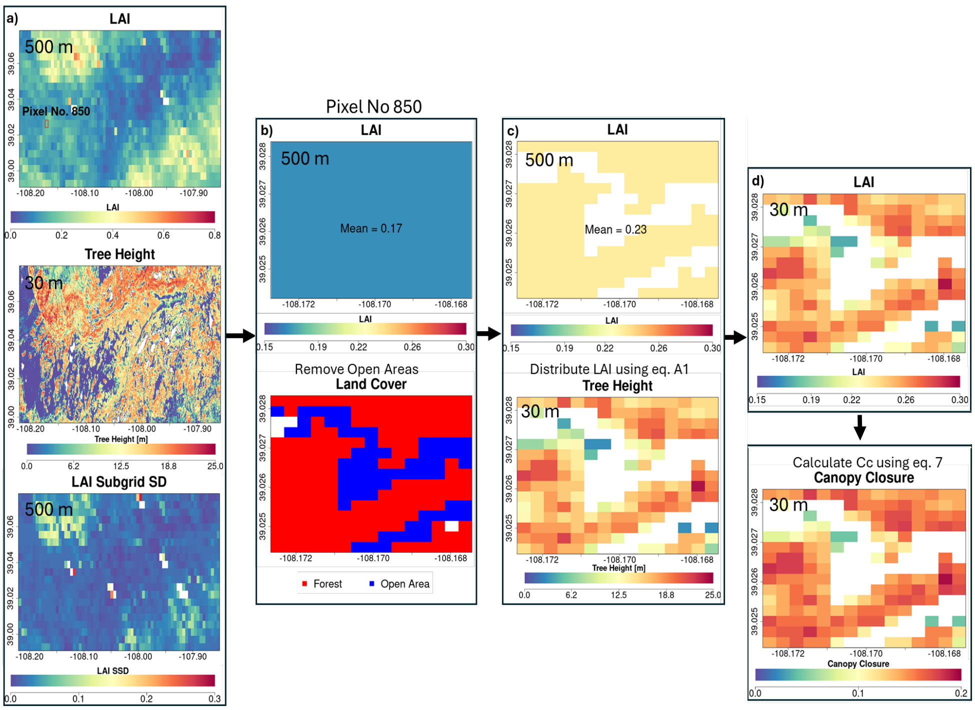

Figure C.1 – Example of downscaling workflow from 500m to 30 m for one MODIS LAI pixel with mixed landcover and estimation of canopy closure: a) MODIS LAI dataset at 500 m, tree height dataset at 30 m, subgrid scale standard deviation (SSD) for the 500 m MODIS pixel. b) LAI and landcover distribution for Pixel No. 850. c) adjusted LAI after removing open areas. d) Redistribution and sampling of LAI using adjusted mean/standard deviation (Eq. C.1) and tree height as spatial covariate to generate the canopy closure at 30 m (Eq. A.3). Open area in Grand Mesa, CO refers to grassland.

D. Retrieved Vegetation Parameters

WCM parameters retrieved in last step (Step IV, Fig. 4) for all available frequencies and polarizations are examined here. Spatial distributions of the mean of the posterior distributions of the retrieved parameters *A* and *B* are presented in Figures D.1 and D.2, respectively. Figure D.3 illustrates the comparison of retrievals for pixels common to two different flight lines acquired at distinct viewing angles. Overall, the retrieved parameters show strong agreement between flights, with the exception of parameter *A* for the X-band VV polarization, which exhibits greater variability. Figure D.4 presents the spatial distribution and cross-flight comparison of the retrieved vegetation water content (Mv), further demonstrating consistency across overlapping observations.

To further quantify cross-flight consistency, Figure D.5 shows the spatial distribution of absolute relative differences, for all retrieved vegetation parameters for all collocated pixels between the two flights. Collocated pixels are identified based on the positions of the pixel centroids. Differences are small (<10–20%) and spatially coherent along the flight

https://doi.org/10.5194/egusphere-2026-3588
Preprint. Discussion started: 4 August 2026

track, increasing only near forest edges or terrain breaks where canopy heterogeneity is strongest. Poor agreement is present for A-Ku (VV) which needs to be studied further.

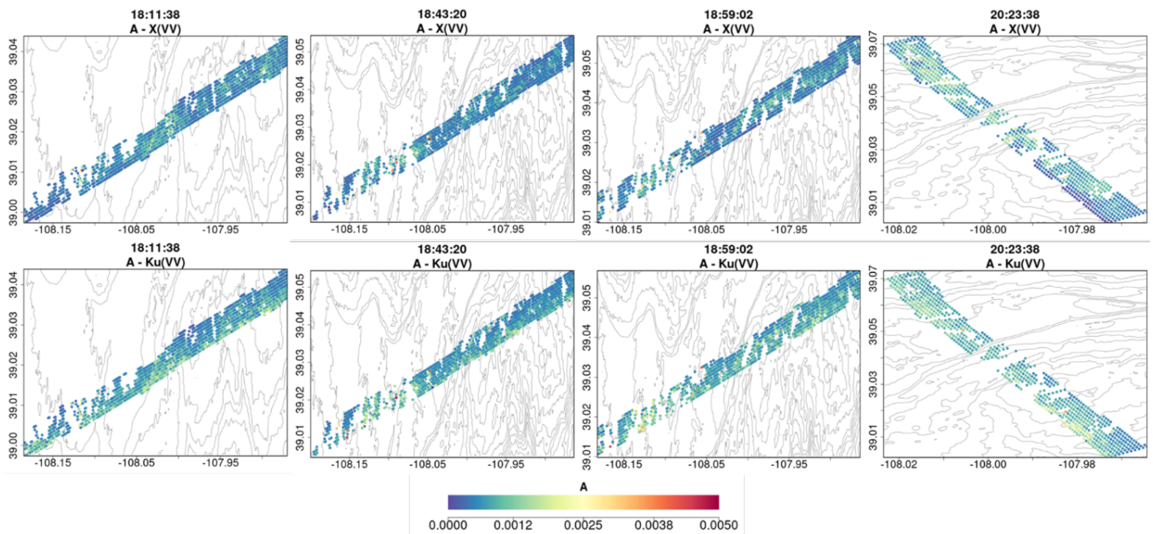

Figure D.1 Spatial plot of WCM parameter A for both channels (X and Ku VV) after final optimization run. Flight times are in UTC.

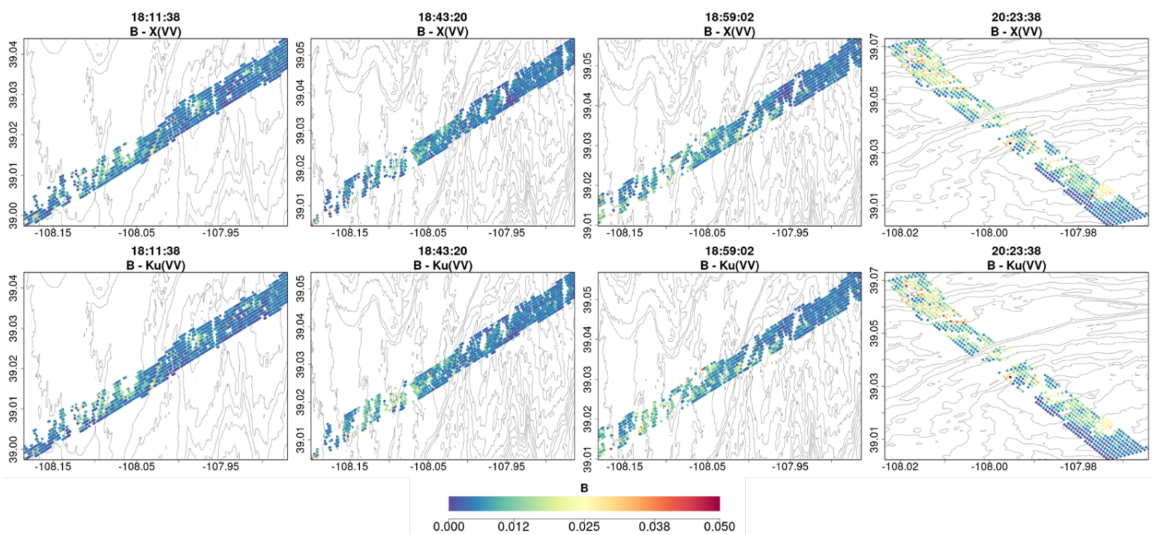

Figure D.2 Spatial plot of WCM parameter B for both channels (X and Ku VV) after final optimization run. Flight times are in UTC.

https://doi.org/10.5194/egusphere-2026-3588
Preprint. Discussion started: 4 August 2026

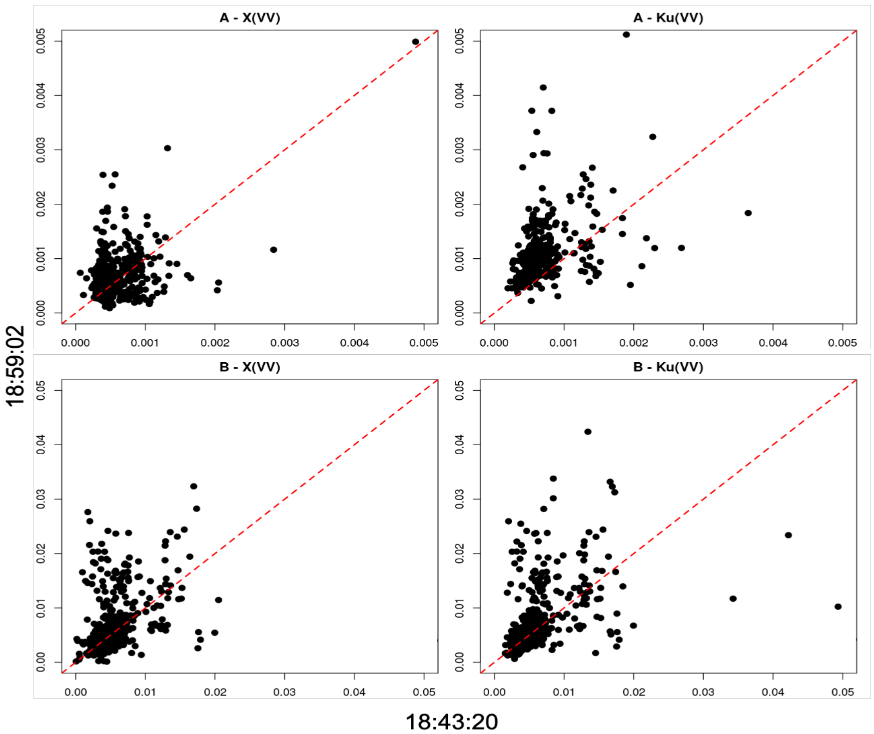

Figure D.3 - Scatterplots of the retrieved A and B parameters from the Water Cloud Model (WCM) for overlapping pixels (based on pixel centroid distance) between the SnowSAR flights at 18:43:20 and 18:59:02 on 23 February 2017. The A parameter represents the canopy attenuation coefficient, while B represents the vegetation scattering term. Each panel shows results for X- and Ku-band VV polarization. Flight times are in UTC.

https://doi.org/10.5194/egusphere-2026-3588
Preprint. Discussion started: 4 August 2026

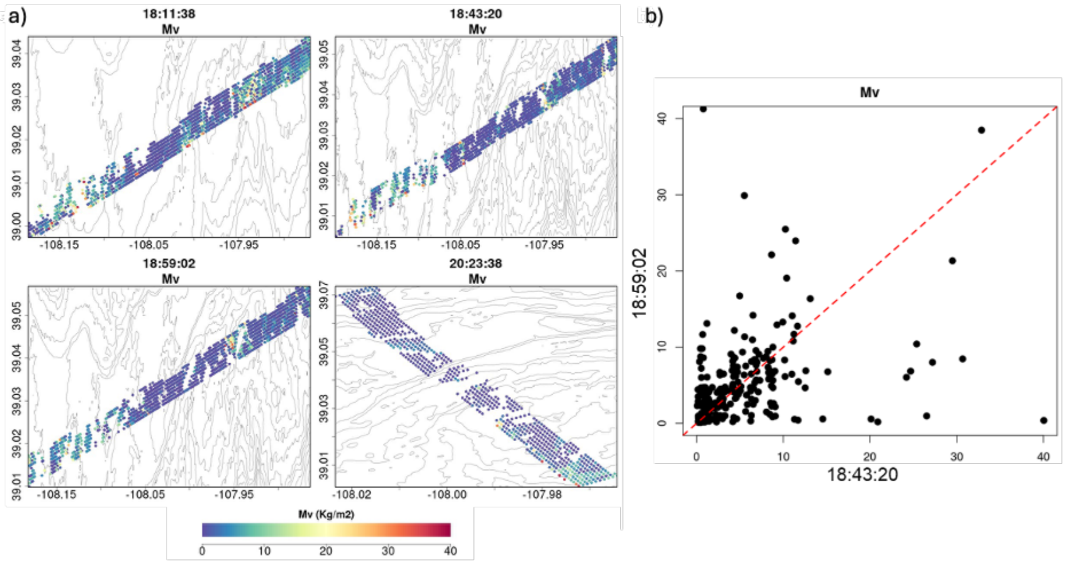

Figure D.4 – a) Spatial distribution of retrieved vegetation water content (*Mv*, kg m⁻²) from four consecutive SnowSAR flights on 23 February 2017 over Grand Mesa, Colorado, showing consistent flight-line coverage and temporal changes in canopy wetness. (b) Scatterplot of *Mv* for overlapping pixels between the 18:43:20 and 18:59:02 flights, illustrating cross-flight consistency of the retrieved vegetation water content. Flight times are in UTC.

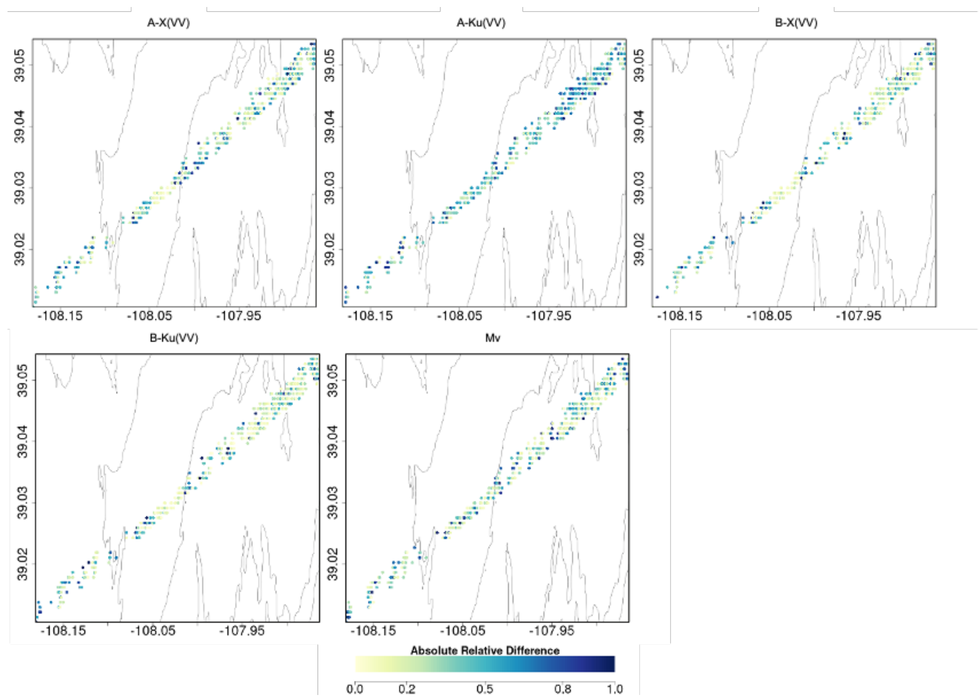

Figure D.5 - Absolute relative differences between frequency and polarization dependent vegetation parameters at collocated pixels of the two consecutive SnowSAR flights (18:43:20 and 18:59:02) for A-X, A-Ku, B-X, B-Ku from Step IV, and *Mv* from Step III demonstrating the importance of incidence angle and viewing geometry for airborne measurements. Areas with the smallest difference (yellow tones) correspond to areas of high homogeneity in Fig. 13. Flight times are in UTC.

https://doi.org/10.5194/egusphere-2026-3588
Preprint. Discussion started: 4 August 2026

E. Residual Backscatter

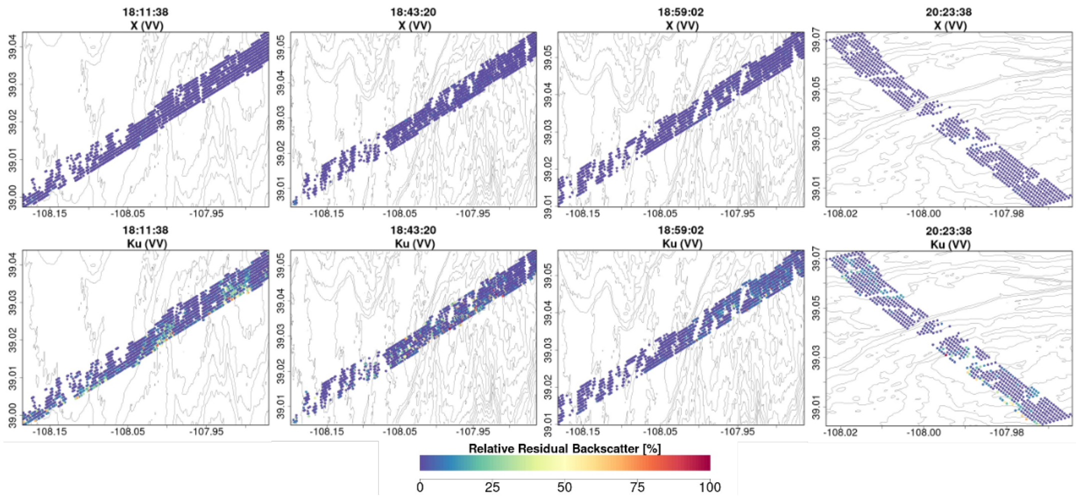

Figure E.1 - Relative residual backscatter (%) for X-band (top row) and Ku-band (bottom row) VV acquisitions at four overpass times. Colors indicate the magnitude of the normalized backscatter residual with respect to model predictions. Most pixels fall below ~10% error, while a limited number of higher-residual pixels appear primarily along forest edges in Ku-band, where vegetation structure drives greater sub-pixel variability. These results support the choice of a 30% residual threshold, which preserves physically meaningful signals. Flight times are in UTC.

F. Abbreviations

ADP- Average distance from all pits

APFF - Average Pit Forest Fraction

LAI – Leaf Area Index

DEM – Digital Elevation Model

RMSE – Root Mean Square Error

R^2 – Coefficient of Determination

MSE – Mean Squared Error

ARD – Absolute Relative Difference

NALCMS – North American Land Change Monitoring System

SAR – Synthetic Aperture Radar

SnowSAR – Dual-frequency (X/Ku) airborne SAR instrument

MSHM – Multilayered Snow Hydrology Model

MEMLS – Microwave Emission Model of Layered Snowpacks

WCM – Water Cloud Model

RTM – Radiative Transfer Model

Base-AM – Bayesian Active Microwave retrieval framework

https://doi.org/10.5194/egusphere-2026-3588
Preprint. Discussion started: 4 August 2026

MCMC – Markov Chain Monte Carlo

HRRR – High-Resolution Rapid Refresh atmospheric model

NWP – Numerical Weather Prediction

LiDAR – Light Detection and Ranging

IEM – Integral Equation Model (microwave scattering)

RRB – Relative Residual Backscatter

BC – Bhattacharyya Coefficient

NLDAS – North American Land Data Assimilation System

GLAD – Global Land Analysis & Discovery tree-height dataset

Ku-band – Ku-band radar frequency (~13–18 GHz)

X-band – X-band radar frequency (~8–12 GHz)

HH, VV, HV – Radar polarization channels (horizontal/vertical)

Symbols

σ_{total} – Total Reflectance within a mixed pixel

σ_{vol} – Volume backscatter from within the snowpack

σ_{bkg} – Background backscatter at the snow–ground interface

σ_{veg} – Vegetation backscatter

ρ – Snow Density

Dz – Snow depth

Q - Cross-polarization fraction used in MEMLS/Base-AM

C_c - Canopy-closure fraction

A, B - WCM parameters

Mv – Vegetation Water Content

SW - Shortwave Radiation

LW - Longwave Radiation

ϵ_v- Vegetation Emmissivity

I- Interception

P_i- Precipitation

f_u – Wind Unloading

f_m – Melt Unloading

l_{ex} – Correlation Length

τ - Transmissivity

Acknowledgements

The authors gratefully acknowledge the insightful feedback provided by the Barros Research Group at the University of Illinois. Additionally, the authors extend their appreciation to the dedicated scientists, engineers, and technicians at

NASA, USGS, ASO, Finnish Met. Institute and Canada Meteorological Service, for their hard work in making valuable satellite datasets freely available.

Code/Data availability

Code will be available upon request to the corresponding author. Input data is publicly available as shown in Table 1

Author contributions

APB and SS conceptualized the study. SS developed and implemented the retrieval framework, including modifications and coupling of the codes, under the guidance of APB. SS completed the retrievals and analyzed the results under the guidance of APB and CV. SS wrote the first draft of the manuscript; APB, and CV edited and revised the manuscript. SS, APB, and CV will reply to the reviewers.

Financial support

This research has been supported by the National Aeronautics and Space Administration (grant no. NNX17AL44G to Ana P. Barros) and the National Oceanic and Atmospheric Administration Cooperative Institute for Research to Operations in Hydrology (CIROH) agreement (grant no. NA22NWS4320003 to Ana P. Barros).

Competing interests. At least one of the (co-)authors is a member of the editorial board of The Cryosphere.

References

Aoki, T., Hachikubo, A., Hori, M., 2000. Effects of snow physical parameters on spectral albedo and bidirectional reflectance of snow surface. J. Geophys. Res. Atmos. 105, 10219–10236. https://doi.org/10.1029/1999JD901122

Asner, G. P., Wessman, C. A., & Archer, S. (1998). Scale dependence of absorption of photosynthetically active radiation in terrestrial ecosystems. Ecological Applications, 8(4), 1003–1021.

Attema, E.P.W., & Ulaby, F.T. (1978). Vegetation modeled as a water cloud. Radio Science, 13(2), 357–364. https://doi.org/10.1029/RS013i002p00357

Baghdadi, N., Cresson, R., El Hajj, M., Ludwig, R., La Jeunesse, I., 2012. Estimation of soil parameters over bare agriculture areas from C-band polarimetric SAR data using neural networks. Hydrol. Earth Syst. Sci. 16, 1607–1621. https://doi.org/10.5194/hess-16-1607-2012

Benjamin, S.G., Weygandt, S.S., Brown, J.M., Hu, M., Alexander, C.R., Smirnova, T.G., Olson, J.B., et al., 2016. A North American hourly assimilation and model forecast cycle: The Rapid Refresh. Mon. Weather Rev. 144, 1669–1694. https://doi.org/10.1175/MWR-D-15-0242.1

Bhattacharyya, A., 1943. On a measure of divergence between two statistical populations defined by their probability distributions. Bull. Calcutta Math. Soc. 35, 99–109

Bindlish, R., Barros, A.P., 2000. Multifrequency soil moisture inversion from SAR measurements with the use of IEM. Remote Sens. Environ. 71, 67–88. https://doi.org/10.1016/S0034-4257(99)00065-6

Bindlish, R., and Barros, A. P. 2001. Parameterization of vegetation backscatter in radar-based soil moisture estimation, Remote Sens. Environ., 76, 130–137, https://doi.org/10.1016/S0034-4257(00)00200-5

Bonnell, R., Elder, K., McGrath, D., Marshall, H.P., Starr, B., Adebisi, N., Palomaki, R.T., Hoppinen, Z., 2024. L-band InSAR snow water equivalent retrieval uncertainty increases with forest cover fraction. Geophys. Res. Lett. 51, e2024GL111708. https://doi.org/10.1029/2024GL111708

Bouchard, B., Nadeau, D.F., Domine, F., Wever, N., Michel, A., Lehning, M., Isabelle, P.-E., 2024. Impact of intercepted and sub-canopy snow microstructure on snowpack response to rain-on-snow events under a boreal canopy. The Cryosphere 18, 2783–2807. https://doi.org/10.5194/tc-18-2783-2024

Boueshagh, M., Ramage, J.M., Brodzik, M.J., Long, D.G., Hardman, M., Marshall, H.-P., 2025. Revealing causes of a surprising correlation: snow water equivalent and spatial statistics from Calibrated Enhanced-Resolution Brightness

https://doi.org/10.5194/egusphere-2026-3588
Preprint. Discussion started: 4 August 2026

Temperatures (CETB) using interpretable machine learning and SHAP analysis. Front. Remote Sens. 6, 1554084. https://doi.org/10.3389/frsen.2025.1554084

Boyd, D.R., Alam, A.M., Kurum, M., Gurbuz, A.C., Osmanoglu, B., 2022. Preliminary snow water equivalent retrieval of SnowEX20 SWESARR data. In: IGARSS 2022 – IEEE Int. Geosci. Remote Sens. Symp., 3927–3930. https://doi.org/10.1109/IGARSS46834.2022.9883412

Cao, Y., Barros, A.P., 2020. Weather-dependent nonlinear microwave behavior of seasonal high-elevation snowpacks. Remote Sens. 12, 3422. https://doi.org/10.3390/rs12203422

Cao, Y., Barros, A.P., 2023. Topographic controls on active microwave behavior of mountain snowpacks. Remote Sens. Environ. 284, 113373. https://doi.org/10.1016/j.rse.2022.113373

Cho, E., Vuyovich, C.M., Kumar, S.V., Wrzesien, M.L., Kim, R.S., 2023. Evaluating the utility of active microwave observations as a snow mission concept using observing system simulation experiments. The Cryosphere 17, 3915–3931. https://doi.org/10.5194/tc-17-3915-2023

Danson, F.M., Hetherington, D., Morsdorf, F., Koetz, B., Allgöwer, B., 2007. Forest canopy gap fraction from terrestrial laser scanning. IEEE Geosci. Remote Sens. Lett. 4, 157–160. https://doi.org/10.1109/LGRS.2006.887064

Dobson, M. C., & Ulaby, F. T., 2007. Active microwave soil moisture research. IEEE Transactions on Geoscience and Remote Sensing, (1), 23-36.

Deems, J.S., Painter, T.H., Finnegan, D.C., 2013. LiDAR measurement of snow depth: a review. J. Glaciol. 59, 467–479. https://doi.org/10.3189/2013JoG12J154

Dubois, P.C., van Zyl, J., Engman, T., 1995. Measuring soil moisture with active microwave: effect of vegetation. In: 1995 International Geoscience and Remote Sensing Symposium (IGARSS'95): Quantitative Remote Sensing for Science and Applications, vol. 1. IEEE, pp. –. https://doi.org/10.1109/36.406677

El Hajj, M., Baghdadi, N., Zribi, M., Belaud, G., Cheviron, B., Courault, D., Charron, F., 2016. Soil moisture retrieval over irrigated grassland using X-band SAR data. Remote Sens. Environ. 176, 202–218. https://doi.org/10.1016/j.rse.2016.01.027

Engineering ToolBox, 2003. Emissivity coefficients of common materials. The Engineering ToolBox. (accessed 23 September 2024)

English, J.M., Turner, D.D., Alcott, T.I., Moninger, W.R., Bytheway, J.L., Cifelli, R., Marquis, M., 2021. Evaluating operational and experimental HRRR model forecasts of atmospheric river events in California. Weather Forecast. 36, 1925–1944.

Essery, R., Mazzotti, G., Barr, S., Jonas, T., Quaife, T., Rutter, N., 2024. A Flexible Snow Model (FSM 2.1.0) including a forest canopy. EGUsphere [preprint] 1–37. https://doi.org/10.5194/egusphere-2024-2546

Essery, R., Pomeroy, J., Ellis, C., Link, T., 2008. Modelling longwave radiation to snow beneath forest canopies using hemispherical photography or linear regression. Hydrol. Process. 22, 2788–2800. https://doi.org/10.1002/hyp.6930

Falk, M., Lin, X., 2021. Time-varying impact of snow depth on tourism in selected regions. Int. J. Biometeorol. 65, 645–657.

Fassnacht, S.R., Cherry, M.L., Venable, N.B.H., Saavedra, F., 2016. Snow and albedo climate change impacts across the United States Northern Great Plains. The Cryosphere 10, 329–339.

Gardner, A.S., Moholdt, G., Cogley, J.G., Wouters, B., Arendt, A.A., Wahr, J., Berthier, E., Hock, R., Pfeffer, W.T., Kaser, G., Ligtenberg, S.R.M., Bolch, T., Sharp, M.J., Hagen, J.O., van den Broeke, M.R., Paul, F., 2013. A reconciled estimate of glacier contributions to sea level rise: 2003 to 2009. Science 340, 852-857. https://doi.org/10.1126/science.1234532

Gottlieb, A.R., Mankin, J.S., 2024. Evidence of human influence on Northern Hemisphere snow loss. Nature 625, 293–300. https://doi.org/10.1038/s41586-023-06794-y

https://doi.org/10.5194/egusphere-2026-3588
Preprint. Discussion started: 4 August 2026

Hall, D.K., Kelly, R.E.J., Foster, J.L., Chang, A.T.C., 2004. Hydrological application of remote sensing: Surface states – snow. NASA Technical Report NTRS 20040034263. (accessed 23 September 2024).

Hardy, J.P., Melloh, R., Koenig, G., Marks, D., Winstral, A., Pomeroy, J.W., Link, T., 2004. Solar radiation transmission through conifer canopies. Agric. For. Meteorol. 126, 257–270.

Hardy, J.P., Davis, R.E., Jordan, R., Ni, W., Woodcock, C.E., 1998. Snow ablation modelling in a mature aspen stand of the boreal forest. Hydrol. Process. 12, 1763–1778.

Hedstrom, N.R., Pomeroy, J.W., 1998. Measurements and modelling of snow interception in the boreal forest. Hydrol. Process. 12, 1611–1625.

Helbig, N., Moeser, D., Teich, M., Vincent, L., Lejeune, Y., Sicart, J.-E., Monnet, J.-M., 2020. Snow processes in mountain forests: interception modeling for coarse-scale applications. Hydrol. Earth Syst. Sci. 24, 2545–2560.

Hernanz, C. (2024). On the limitations of deep learning for statistical downscaling of climate change projections: The transferability and the extrapolation issues. Atmos. Sci. Lett., https://doi.org/10.1002/asl.1195

Horrigan, T., Bates, R.E., 1995. Estimated snow parameters for vehicle mobility modeling in Korea, Germany and interior Alaska. Spec. Rep. 95-23, U.S. Army Cold Regions Research and Engineering Laboratory, Hanover, NH. https://apps.dtic.mil/sti/tr/pdf/ADA301154.pdf

Jacobs, J.M., Hunsaker, A.G., Sullivan, F.B., Palace, M., Burakowski, E.A., Herrick, C., Cho, E., 2021. Snow depth mapping with unpiloted aerial system lidar observations: a case study in Durham, New Hampshire, United States. The Cryosphere 15, 1485–1500.

James, E. P., Alexander, C. R., Dowell, D. C., Weygandt, S. S., Benjamin, S. G., Manikin, G. S., Brown, J. M., et al.: The High-Resolution Rapid Refresh (HRRR): an hourly updating convection-allowing forecast model. Part II: Forecast performance, 2022. Weather Forecast., 37, 1397–1417, https://doi.org/10.1175/WAF-D-21-0130.1

Jennings, K.S., Molotch, N.P., 2020. Snowfall fraction, cold content, and energy balance changes drive differential response to simulated warming in an alpine and subalpine snowpack. Front. Earth Sci. 8, 186.

Kacimi, S., Kwok, R., 2022. Arctic snow depth, ice thickness, and volume from ICESat-2 and CryoSat-2: 2018-2021. Geophysical Research Letters 49, e2021GL097448. https://doi.org/10.1029/2021GL097448

Kang, D.H., Barros, A.P., 2012. Observing system simulation of snow microwave emissions over data-sparse regions – Part I: Single-layer physics. IEEE Trans. Geosci. Remote Sens. 50, 1785–1805. https://doi.org/10.1109/TGRS.2011.2169073

Kang, D.H., Barros, A.P., 2012. Observing system simulation of snow microwave emissions over data-sparse regions – Part II: Multilayer physics. IEEE Trans. Geosci. Remote Sens. 50, 1806–1820. https://doi.org/10.1109/TGRS.2011.2169074

Khabazan, S., Motagh, M., Hosseini, M., 2013. Evaluation of radar backscattering models IEM, Oh, and Dubois using L- and C-band SAR data over different vegetation canopy covers and soil depths. Int. Arch. Photogramm. Remote Sens. Spatial Inf. Sci. XL-1/W3, 225–230.

Kumar, K., Prasad, K.S.H., Arora, M.K., 2012. Estimation of Water Cloud Model vegetation parameters using a genetic algorithm. Hydrol. Sci. J. 57, 776–789. https://doi.org/10.1080/02626667.2012.678583

Lee, S.M., Shi, H., Sohn, B.J., Gasiewski, A.J., Meier, W.N., Dybkjaer, G., 2021. Winter snow depth on Arctic sea ice from satellite radiometer measurements (2003–2020): Regional patterns and trends. Geophys. Res. Lett. 48, e2021GL094541.

Lemmetyinen, J., Ruiz, J.J., Cohen, J., Haapamaa, J., Kontu, A., Pulliainen, J., Praks, J., 2022. Attenuation of radar signal by a boreal forest canopy in winter. IEEE Geosci. Remote Sens. Lett. 19, 1–5. https://doi.org/10.1109/LGRS.2022.3187295

Li, P., Gao, A., Bai, M., Qiu, S., 2025. Evaluation of snow-drifting influencing factors and susceptibility of transportation infrastructure lines. Sci. Rep. 15, 2434. https://doi.org/10.1038/s41598-025-86207-4

https://doi.org/10.5194/egusphere-2026-3588
Preprint. Discussion started: 4 August 2026

Li, D., Durand, M., Margulis, S.A., 2017. Estimating snow water equivalent in a Sierra Nevada watershed via spaceborne radiance data assimilation. Water Resour. Res. 53, 647–671. https://doi.org/10.1002/2016WR018878

Li, J., Wang, S., 2018. Using SAR-derived vegetation descriptors in a water cloud model to improve soil moisture retrieval. Remote Sens. 10, 1370. https://doi.org/10.3390/rs10091370

Lim, S., Gim, H.-J., Lee, E., Lee, S.-Y., Lee, W.Y., Lee, Y.H., Cassardo, C., Park, S.K., 2022. Optimization of snow-related parameters in Noah Land Surface Model (v3.4.1) using Micro-Genetic Algorithm (v1.7a). Geosci. Model Dev. 15, 8541–8559. https://doi.org/10.5194/gmd-15-8541-2022

Lundquist, J.D., Dickerson-Lange, S., Gutmann, E., Jonas, T., Lumbrazo, C., Reynolds, D., 2021. Snow interception modelling: Isolated observations have led to many land surface models lacking appropriate temperature sensitivities. Hydrological Processes 35, e14274. https://doi.org/10.1002/hyp.14274

Mahat, V., Tarboton, D.G., 2012. Canopy radiation transmission for an energy balance snowmelt model. Water Resour. Res. 48, W01534.

May, L., Stuefer, S., Goddard, S., Larsen, C., 2025. Analyzing vegetation effects on snow depth variability in Alaska's boreal forests with airborne lidar. The Cryosphere 19, 3477–3492. https://doi.org/10.5194/tc-19-3477-2025

Mazzotti, G., Nousu, J.P., Vionnet, V., Jonas, T., Nheili, R., Lafaysse, M., 2024. Exploring the potential of forest snow modeling at the tree and snowpack layer scale. The Cryosphere 18, 4607–4632. https://doi.org/10.5194/tc-18-4607-2024

Metropolis, N., Rosenbluth, A.W., Rosenbluth, M.N., Teller, A.H. and Teller, E., 1953. Equation of state calculations by fast computing machines. The Journal of Chemical Physics, 21(6), pp.1087-1092.

Mironov, V. L., Kosolapova, L. G., & Fomin, S. V., 2009. Physically and mineralogically based spectroscopic dielectric model for moist soils. IEEE Transactions on Geoscience and Remote Sensing, 47(7), 2059-2070.

Mote, P.W., Hamlet, A.F., Clark, M.P., Lettenmaier, D.P., 2005. Declining mountain snowpack in western North America. Bull. Am. Meteorol. Soc. 86, 39–50.

Mueller, M.M., Dubois, C., Jagdhuber, T., Hellwig, F.M., Pathe, C., Schmullius, C., Steele-Dunne, S., 2022. Sentinel-1 backscatter time series for characterization of evapotranspiration dynamics over temperate coniferous forests. Remote Sens. 14, 6384. https://doi.org/10.3390/rs14246384

Myneni, R.B., Ross, J., Asrar, G., 1989. A review on the theory of photon transport in leaf canopies. Agric. For. Meteorol. 45, 1–153.

Myneni, R., Knyazikhin, Y., Park, T., 2015. MOD15A2H MODIS/Terra Leaf Area Index/FPAR 8-Day L4 Global 500 m SIN Grid V006 [dataset]. NASA EOSDIS Land Processes DAAC, v006.

National Academies of Sciences, Engineering, and Medicine (NASEM), 2018. Thriving on Our Changing Planet: A Decadal Strategy for Earth Observation from Space. The National Academies Press, Washington, DC. https://doi.org/10.17226/24938

Nicolaus, M., Hoppmann, M., Arndt, S., Hendricks, S., Katlein, C., Nicolaus, A., Rossmann, L., Schiller, M., Schwegmann, S., 2021. Snow depth and air temperature seasonality on sea ice derived from snow buoy measurements. Front. Mar. Sci. 8, 655446.

Oh, Y., Chang, J.G., Shoshany, M., 2022. An empirical model for backscattering coefficients of vegetation fields at 5.4 GHz. J. Electromagn. Eng. Sci. 22, 146–151.

Painter, T.H., 2018. ASO L4 Lidar Snow Water Equivalent 50m UTM Grid, Version 1. NASA National Snow and Ice Data Center DAAC, Boulder, Colorado USA. https://doi.org/10.5067/M4TUH28NHL4Z

Pan, J., Durand, M., Lemmetyinen, J., Liu, D., Shi, J., 2024. Snow water equivalent retrieved from X- and dual Ku-band scatterometer measurements at Sodankylä using the Markov Chain Monte Carlo method. The Cryosphere 18, 1561–1578. https://doi.org/10.5194/tc-18-1561-2024, 2024

https://doi.org/10.5194/egusphere-2026-3588
Preprint. Discussion started: 4 August 2026

Panciera, R., Tanase, M.A., Lowell, K., Walker, J.P., 2013. Evaluation of IEM, Dubois, and Oh radar backscatter models using airborne L-band SAR. IEEE Trans. Geosci. Remote Sens. 52, 4966–4979. https://doi.org/10.1109/TGRS.2013.2286203

Park, S.-E., Jung, Y.T., Cho, J.-H., Moon, H., Han, S., 2019. Theoretical evaluation of Water Cloud Model vegetation parameters. Remote Sens. 11, 894.

Peng, R., Yan, K., Liu, J., Gao, S., Pu, J., Maeda, E.E., Zhu, P., Knyazikhin, Y., Myneni, R.B., 2024. Revisiting the consistency of MODIS LAI products from a new perspective of spatiotemporal variability. Int. J. Digit. Earth 17, 2407045.

Pomeroy, J.W., Gray, D.M., Hedstrom, N.R., Janowicz, J.R., 2002. Prediction of seasonal snow accumulation in cold climate forests. Hydrol. Process. 16, 3543–3558.

Pongracz, A., Wårlind, D., Miller, P.A., Gustafson, A., Rabin, S.S., Parmentier, F.-J.W., 2024. Warming-induced contrasts in snow depth drive the future trajectory of soil carbon loss across the Arctic–Boreal region. Commun. Earth Environ. 5, 684. https://doi.org/10.1038/s43247-024-01838-1

Potapov, P., Hansen, M.C., Kommareddy, I., Kommareddy, A., Turubanova, S., Pickens, A., Adusei, B., Tyukavina, A., Ying, Q., 2020. Landsat analysis ready data for global land cover and land cover change mapping. Remote Sens. 12, 426.

Proksch, M., Mätzler, C., Wiesmann, A., Lemmetyinen, J., Schwank, M., Löwe, H., & Schneebeli, M. (2015). MEMLS3&a: Microwave Emission Model of Layered Snowpacks adapted to include backscattering. Geoscientific Model Development, 8(8), 2611–2626. https://doi.org/10.5194/gmd-8-2611-2015

Qin, X., Pang, Z., Lu, J., 2024. Estimation and analysis of vegetation parameters for the Water Cloud Model. River 3, 399–407. https://doi.org/10.1002/rvr2.103

Rasmus, S., Gustafsson, D., Koivusalo, H., Laurén, A., Grelle, A., Kauppinen, O.-K., Lagnvall, O., Lindroth, A., Rasmus, K., Svensson, M., Weslien, P., 2013. Estimation of winter leaf area index and sky view fraction for snow modelling in boreal coniferous forests: consequences on snow mass and energy balance. Hydrol. Process. 27, 2876–2891.

Rodell, M., Houser, P.R., 2004. Updating a land surface model with MODIS-derived snow cover. J. Hydrometeorol. 5, 1064–1075.

Sabetghadam, S., Fletcher, C.G., Erler, A., 2025. The importance of model horizontal resolution for improved estimation of snow water equivalent in a mountainous region of western Canada. Hydrol. Earth Syst. Sci. 29, 887–902.

Seidel, D., Ruzicka, K.J., Puettmann, K., 2016. Canopy gaps affect the shape of Douglas-fir crowns in the western Cascades, Oregon. For. Ecol. Manage. 363, 31–38.

Sellers, P.J., 1985. Canopy reflectance, photosynthesis and transpiration. Int. J. Remote Sens. 6, 1335–1372.

Sellers, P.J., 1987. Canopy reflectance, photosynthesis, and transpiration. II. The role of biophysics in the linearity of their interdependence. Remote Sens. Environ. 21, 143–183.

Semadeni-Davies, A., 2004. Urban water management vs. climate change: Impacts on cold region wastewater inflows. Climatic Change 64, 103-126. https://doi.org/10.1023/B:CLIM.0000024669.22066.04

Shi, S., Liu, G., 2021. The latitudinal dependence in the trend of snow event to precipitation event ratio. Sci. Rep. 11, 18112. https://doi.org/10.1038/s41598-021-97451-9

Singh, S., Durand, M., Kim, E., Barros, A.P., 2024. Bayesian physical–statistical retrieval of snow water equivalent and snow depth from X- and Ku-band synthetic aperture radar – demonstration using airborne SnowSAR in SnowEx'17. The Cryosphere 18, 747–773.

Slater, L., Dios, V., & Montanari, A. (2025). Challenges and opportunities of machine learning and explainable AI in large-sample hydrology. Philos. Trans. R. Soc. A, 383, 20240287.

https://doi.org/10.5194/egusphere-2026-3588
Preprint. Discussion started: 4 August 2026

Sthapit, E., Lakhankar, T., Hughes, M., Khanbilvardi, R., Cifelli, R., Mahoney, K., Currier, W.R., Viterbo, F., Rafieeinasab, A., 2022. Evaluation of snow and streamflows using Noah-MP and WRF-Hydro models in Aroostook River basin, Maine. Water 14, 2145.

Storck, P., Lettenmaier, D.P., Bolton, S.M., 2002. Measurement of snow interception and canopy effects on snow accumulation and melt in a mountainous maritime climate, Oregon, United States. Water Resour. Res. 38, 1223. https://doi.org/10.1029/2002WR001281

Sturm, M., Taras, B., Liston, G.E., Derksen, C., Jonas, T., Lea, J., 2010. Estimating snow water equivalent using snow depth data and climate classes. J. Hydrometeorol. 11, 1380–1394.

Switanek, M., Resch, G., Gobiet, A., Günther, D., Marty, C., Schöner, W., 2024. Snow depth sensitivity to mean temperature, precipitation, and elevation in the Austrian and Swiss Alps. The Cryosphere 18, 6005–6026.

Tsang, L., Pan, J., Liang, D., Li, Z., Cline, D. W., and Tan, Y., 2007. Modeling active microwave remote sensing of snow using dense media radiative transfer (DMRT) theory with multiple-scattering effects, IEEE Trans. Geosci. Remote Sens., 45, 990–1004, https://doi.org/10.1109/TGRS.2006.888854

Tsang, L., Durand, M., Derksen, C., Barros, A.P., Kang, D.-H., Lievens, H., Marshall, H.-P., Zhu, J., Johnson, J., King, J., Lemmetyinen, J., Sandells, M., Rutter, N., Siqueira, P., Nolin, A., Osmanoglu, B., Vuyovich, C., Kim, E., Taylor, D., … Xu, X., 2022. Review article: Global monitoring of snow water equivalent using high-frequency radar remote sensing. The Cryosphere 16, 3531–3573. https://doi.org/10.5194/tc-16-3531-2022

Urrego, J.P.F., Huang, B., Sandstad Næss, J., Hu, X., Cherubini, F., 2021. Meta-analysis of leaf area index, canopy height and root depth of three bioenergy crops and their effects on land surface modeling. Agric. For. Meteorol. ,306, 108444.

Vermunt, P.C., Steele-Dunne, S.C., Khabbazan, S., Kumar, V., Judge, J., 2022. Towards understanding the influence of vertical water distribution on radar backscatter from vegetation using a multi-layer water cloud model. Remote Sens. 14, 3867.

Wang, K., Wang, P., Li, Z., Cribb, M., Sparrow, M., 2007. A simple method to estimate actual evapotranspiration from a combination of net radiation, vegetation index, and temperature. J. Geophys. Res. Atmos. 112, D15107. https://doi.org/10.1029/2006JD008351

Wang, R., Chen, J.M., Pavlic, G., Arain, A., 2016. Improving winter leaf area index estimation in coniferous forests and its significance in estimating the land surface albedo. ISPRS J. Photogramm. Remote Sens. 119, 32–48. https://doi.org/10.1016/j.isprsjprs.2016.05.003

Wiesmann, A., Hatzler, C., & Hiltbrunner, D., 1998. Modeling microwave emission spectra of layered snowpacks. In IGARSS'98. Sensing and Managing the Environment. 1998 IEEE International Geoscience and Remote Sensing. Symposium Proceedings.(Cat. No. 98CH36174) (Vol. 3, pp. 1265-1267). IEEE.

Wrzesien, M.L., Durand, M.T., Pavelsky, T.M., Howat, I.M., Margulis, S.A., Huning, L.S., 2017. Comparison of methods to estimate snow water equivalent at the mountain range scale: A case study of the California Sierra Nevada. J. Hydrometeorol. 18, 1101–1119.

Xu, L., Dirmeyer, P., 2013. Snow–atmosphere coupling strength. Part II: Albedo effect versus hydrological effect. J. Hydrometeorol. 14, 404–418. https://doi.org/10.1175/JHM-D-11-0103.1

Yuan, Y.; Wang, X.; Yin, F.; Zhan, J.: "Examination of the quantitative relationship between vegetation canopy height and LAI," Advances in Meteorology, 2013, Article ID 964323, 6 pp., https://doi.org/10.1155/2013/964323

Zhu, J., Tan, S., Tsang, L., Kang, D.-H., Kim, E., 2021. Snow water equivalent retrieval using active and passive microwave observations. Water Resour. Res. 57, e2020WR027563.